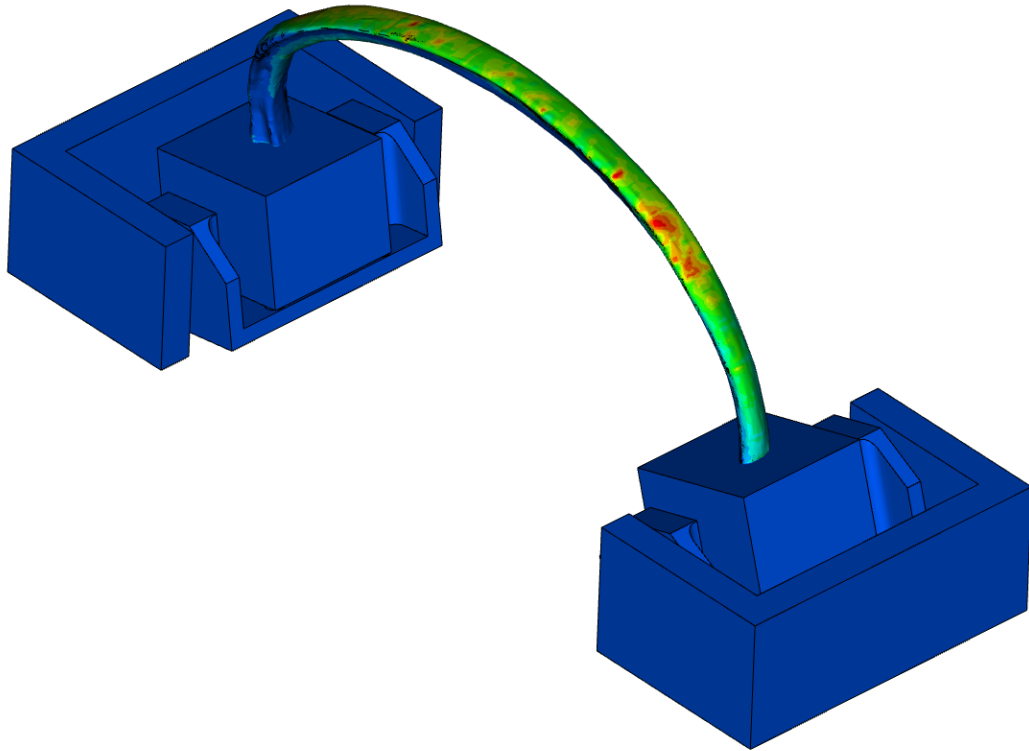




**CHALMERS**  
UNIVERSITY OF TECHNOLOGY

---



# Detailed FE rib modelling for fracture prediction

Master's thesis in Applied Mechanics

LINUS LUNDIN  
SIMON STORM



MASTER'S THESIS 2018

# Detailed FE rib modelling for fracture prediction

LINUS LUNDIN  
SIMON STORM



**CHALMERS**

Department of Mechanics and Maritime Sciences  
CHALMERS UNIVERSITY OF TECHNOLOGY  
Gothenburg, Sweden 2018

Detailed FE rib modelling for fracture prediction  
LINUS LUNDIN  
SIMON STORM

© LINUS LUNDIN, SIMON STORM, 2018.

Supervisor: Johan Iraeus, PhD, Mechanics and Maritime Sciences  
Supervisor: Bengt Pipkorn, Adjunct Professor, Mechanics and Maritime Sciences &  
Autoliv Inc.  
Examiner: Johan Davidsson. PhD, Mechanics and Maritime Sciences

Master's Thesis 2018:97  
Department of Mechanics and Maritime Sciences  
Chalmers University of Technology  
SE-412 96 Gothenburg  
Sweden  
Telephone +46 31 772 1000

Cover: 1<sup>st</sup> principal strain concentration indicating the fracture location in Rib  
specimen J.

Typeset in L<sup>A</sup>T<sub>E</sub>X  
Department of Mechanics and Maritime Sciences  
Gothenburg, Sweden 2018

Detailed FE rib modelling for fracture prediction  
Master's thesis in Applied Mechanics  
LINUS LUNDIN  
SIMON STORM  
Department of Mechanics and Maritime Sciences  
Chalmers University of Technology

## Abstract

The purpose of this thesis was to investigate if rib fracture can be predicted in dynamic analysis using the first principal strain estimate on subject specific finite element (FE) models of human ribs. The investigation was first to be conducted on models represented by an all hexahedral (all-hex) element based mesh. If the rib fracture was captured with a detailed all-hex modeling approach, the aim was to determine what would be the maximum level of simplification that could be used in the FE model, without losing the capability to estimate the fracture location.

Subject specific FE models were developed to reproduce dynamic end-to-end rib displacement tests, conducted prior to this thesis, on twelve number sixth rib specimens. Pre-test, high resolution CT images of the rib geometries were taken to be individually processed with a cortical bone mapping algorithm to provide subject specific cortical bone thickness. The thickness distributions enabled a manual Hexa-Block meshing procedure of the cortical and trabecular bone of the ribs. The all-hex meshed cortical bone was in a later step converted to, eight node thick shell elements, followed by quadrilateral shell elements with nodal thicknesses. Material tension tests were conducted on coupons of the cortical bone to provide subject specific isotropic material properties. Isotropic linear elastic heterogeneous material properties for the rib specimens' trabecular bone were obtained based on density estimates from the same CT data, though processed in an earlier Master's thesis on the same set of rib specimens. In a later step, the heterogeneous material data was also homogenized to a linear elastic isotropic material representation.

Four different modeling approaches were analyzed. The most detailed model used an all-hex mesh with heterogeneous trabecular material properties. The first simplification step used an all-hex mesh with a subject specific homogenized trabecular material property. In the second and third simplification steps, the cortical bone was represented with thick and thin shell elements, respectively. Both employing heterogeneous trabecular material properties.

Because of numerical instabilities unable to be resolved within the timeframe of the project, the thick shell modeling approach failed the energy balance assessment. Hence, the pertaining results were deemed unfeasible to evaluate.

Overall, the model validations showed that seven out of twelve rib models had a non optimized reaction force-displacement response which agreed well with the original experiment. In addition, other metrics measured in the experiment were also accurately captured for the seven ribs, independent of modeling approach (excluding thick shell). However, only the all-hex models accurately captured the correct fracture locations.

The five ribs that did not capture the force-displacement response also did not predict the correct fracture location. The disagreements for the five ribs are hypothesized to be owed to cortical porosity effects. These effects influence the quality of the coupon tension tests as well as the cortical bone mapping algorithm, which lack the ability to correctly represent changes in tissue-level properties due to cortical porosity.

The results imply that the human rib fracture is strain controlled and can be successfully captured in a subject specific finite element model which uses elements supporting a 3D stress state to model the cortical bone. Consequently, the most simplified model to capture the fracture location was an all-hex model with homogeneous material properties. The results provide guidelines for further development of the thorax used in impact biomechanic human body models.

Keywords: Applied Mechanics, Finite Element Method, rib, rib modelling, thesis.



# Acknowledgements

We would first like to thank our thesis supervisor Ph.D Johan Iraeus of the Mechanics and Maritime Sciences at Chalmers and Adjunct Professor Bengt Pipkorn of the Mechanics and Maritime Sciences at Chalmers & Autoliv Inc..

Secondly, we would like to direct our greatest gratitude to Ph.D Milton Peña at the BETA CAE Nordic team. His enthusiasm and devotion in ANSA related assistance has been invaluable to this Master's thesis.

We would also like to thank the experts who were involved in providing material for this research project: Dr. Amanda Agnew, Dr. Andrew R. Kemper and Dr. Sven A. Holcombe.

Lastly, we are grateful to all of you at the SAFER department with whom we have had the pleasure to work with during this period. Your professional guidance has taught us a great deal leading to the finalization of this project.

Linus Lundin & Simon Storm, Gothenburg, December 2018





# Nomenclature

		$E_{\text{tot}}$	Total energy
		$E_{\text{tot}}^0$	Total initial energy
		$f()$	Function of
		$W_{\text{ext}}$	External Work
		AHM	All-Hex Map modeling approach
		AHV	All-Hex Voigt modeling approach
$C$	Damping matrix in equations of motion	all-hex	All Hexahedral mesh of both cortical and trabecular bone
$K$	Stiffness matrix in equations of motion	ANSA	Pre-processor, BETA CAE Systems
$M$	Mass matrix in equations of motion	AR	Aspect Ratio
$\mathbf{u}$	displacement field in equations of motion	CAD	Computer-Aided Design
		CBM	Cortical Bone Mapping
$\Delta t_{\text{min}}$	Critical time step	CFL	Courant–Friedrichs–Lewy condition
$\mathbf{f}$	Load vector in equations of motion	clinCT	Clinical Computed Tomography
$\bar{\rho}^{\text{Voigt}}$	Voigt average density	CORA	COrelation and Analysis software
$\bar{E}^{\text{Voigt}}$	Voigt average Young’s modulus	CT	Computed Tomography
$\rho$	Density	ELFORM	Element formulation
$\sigma^{\text{eng}}$	Engineering stress	FE	Finite Element
$\sigma^{\text{true}}$	True stress	FEM	Finite Element Method
$\varepsilon$	Strain	FFT	Fast Fourier Transform
$\varepsilon^{\text{eng}}$	Engineering strain	HBM	Human Body Model
$\varepsilon^{\text{true}}$	True strain	HG	Hourglass Control
$\varepsilon_{\text{eff, plastic}}^{\text{true}}$	True effective plastic strain	HRclinCT	High Resolution clinical
$E$	Young’s Modulus		

---

	Computed Tomography	tems
HS	Hex-Shell approach	microCT Micro Computed Tomography
HTS	Hex-Thick Shell modeling approach	MPP Message Passing Parallel
HU	Hounsfield Unit	p. cup Potting cup
IOE	Interval of evaluation	PDE Partial Differential Equation
LS-DYNA	Multi-purpose explicit and implicit finite element solver, LSTC	PMHS Post Mortem Human Subject
MATLAB	Multi-paradigm numerical computing environment, Mathworks	RVE Representative Volume Element
META	Post-processor, BETA CAE Sys-	shell-hex Shell mesh of cortical bone, hexahedral mesh of trabecular bone
		std Standard deviation

# Contents

<b>Nomenclature</b>	<b>ix</b>
<b>List of Figures</b>	<b>xiii</b>
<b>List of Tables</b>	<b>xv</b>
<b>1 Introduction</b>	<b>1</b>
1.1 Background . . . . .	1
1.2 Objective . . . . .	2
1.3 Limitations . . . . .	2
1.4 Specification of Issue Under Investigation . . . . .	3
<b>2 Literature Study</b>	<b>5</b>
2.1 Test Procedure . . . . .	5
2.2 Mechanical Properties of Ribs . . . . .	7
2.2.1 Geometrical Properties . . . . .	7
2.2.2 Material Properties . . . . .	9
2.3 FE Modeling of Ribs . . . . .	10
<b>3 Theory</b>	<b>13</b>
3.1 Microscopic Structure of Bones . . . . .	13
3.2 Rib Anatomy . . . . .	14
3.3 Implicit and Explicit Analysis . . . . .	15
3.3.1 The Courant-Friedrichs-Lewy (CFL) Condition . . . . .	16
3.4 Mass and Time Step Scaling . . . . .	17
3.5 Solid Hexahedral Elements . . . . .	18
3.6 Shell Elements . . . . .	18
3.6.1 Thick Shells . . . . .	18
3.6.2 Thin Shells . . . . .	19
3.7 Hourglass Control . . . . .	19
3.8 Mesh Quality . . . . .	20
3.9 Energy Balance . . . . .	21
<b>4 Materials and Methods</b>	<b>23</b>
4.1 Experimental Data for Validation . . . . .	23
4.2 Curve-to-curve Comparison . . . . .	24

4.2.1	CORA . . . . .	24
4.2.2	Paired t-test . . . . .	25
4.3	Fracture Location Metric . . . . .	26
4.4	Solver Controls . . . . .	27
4.5	Simplification Process . . . . .	27
4.5.1	AHM - All-Hex Map approach . . . . .	27
4.5.2	AHV - All-Hex Voigt approach . . . . .	28
4.5.3	HTS - Hex Thick Shell approach . . . . .	28
4.5.4	HS - Hex Shell approach . . . . .	28
4.6	Hexahedral Meshing Procedure . . . . .	28
4.7	Thick Shell Generation . . . . .	31
4.8	Thin Shell Generation . . . . .	31
4.9	Mapping of Trabecular Material Properties . . . . .	32
4.10	Homogenization of Trabecular Material Properties . . . . .	32
4.11	Cortical Material Data Processing . . . . .	33
4.12	Simulation Setup . . . . .	34
4.13	Positioning of Meshed Rib Specimens . . . . .	36
4.14	Sensitivity Analysis of Rotation Axis . . . . .	37
4.15	Average Cortical Thickness . . . . .	37
4.16	Natural Frequency Analysis . . . . .	38
<b>5</b>	<b>Results</b>	<b>39</b>
5.1	Energy Balance and Mass Scaling . . . . .	39
5.2	Hex-Thick Shell Modeling Approach . . . . .	39
5.3	Mesh Quality . . . . .	40
5.4	Sensitivity Analysis of Rotation Axis . . . . .	41
5.5	Force-Displacement Response . . . . .	42
5.6	Rotations . . . . .	45
5.7	Strain-gauges . . . . .	46
5.8	Fracture Location . . . . .	48
5.9	Cortical Thickness . . . . .	51
5.10	Natural Frequency Analysis . . . . .	52
<b>6</b>	<b>Discussion</b>	<b>55</b>
<b>7</b>	<b>Conclusion</b>	<b>59</b>
<b>8</b>	<b>Further Work</b>	<b>61</b>
	<b>Bibliography</b>	<b>65</b>
<b>A</b>	<b>Appendix 1</b>	<b>I</b>
A.1	Energy balance evaluation . . . . .	II
A.2	Simulation-Validation plots . . . . .	III

# List of Figures

2.1	Test rig used to produce experimental data. . . . .	6
2.1a	Photo of side view with strain gauges in green. . . . .	6
2.1b	Iso-view of CAD geometry. . . . .	6
2.2	Typical microCT with perio- and endosteal borders highlighted. Adopted from Fig.2 in [13]. . . . .	8
2.3	CT images of rib cross section captured with three different levels of resolution. Figure adapted from Fig.4 in [13]. . . . .	8
2.4	CT image of rib cross-section with initial boundary, sampled cortical signals and the 6-parameter step model fitted. Adopted from Fig.5 in [13]. . . . .	9
3.1	Illustration of a cross-section cut of a long bone. Figure adopted from [32]. . . . .	13
3.2	Anatomical directional terms with a coordinate system used throughout this thesis . . . . .	14
3.2a	Side-view of thorax. Figure adapted from Fig.114 in [9]. . . . .	14
3.2b	Top and side-view of rib. . . . .	14
3.3	Rib with structural features. Figure adapted from Fig.122 in [9]. . . . .	15
3.4	Illustration of the mesh quality metrics; (a) aspect ratio, (b) angle idealization, and (c) Jacobian . . . . .	21
3.4a	. . . . .	21
3.4b	. . . . .	21
3.4c	. . . . .	21
4.1	Raw and smoothed versions of the endosteal surface of rib specimen H. . . . .	29
4.1a	Raw . . . . .	29
4.1b	Smoothed. . . . .	29
4.2	Endosteal surface with Hexa-Boxes fitted. . . . .	29
4.3	Illustration of how the hexahedral mesh is created, yellow=endosteal surface, blue=trabecular solids, green=periosteal surface, red=cortical solids, light blue=Hexa-Boxes. . . . .	30
4.3a	Exploded view of cross-section. . . . .	30
4.3b	Periosteal and endosteal surfaces. . . . .	30
4.3c	Cortical and trabecular hexahedrals. . . . .	30
4.4	Resulting mesh without and with the use of O-grid. . . . .	30
4.4a	No O-grid, Rib E. . . . .	30

4.4b	O-grid x 4, Rib K. . . . .	30
4.5	Support components including bracket (yellow), potting cup (blue), and pot (red). point <b>C</b> is center of pot and <b>a</b> =8.5 mm is the x-distance from <b>C</b> to rotational axis. . . . .	34
4.6	The simulation setup with posterior left and anterior right. . . . .	35
4.6a	Side view. . . . .	35
4.6b	Top view. . . . .	35
4.7	Hexahedral mesh (red) aligned with laser-scanned mesh (cyan). . . .	36
5.1	Simulation comparison with experiments for rib specimen K. Fracture occurs at 39.35 ms. . . . .	42
5.1a	Force-Displacement, time-shifted . . . . .	42
5.1b	Rotation-Time history. . . . .	42
5.1c	Strain gauge-Time history at 30% of curve length. . . . .	42
5.1d	Strain gauge-Time history at 60% of curve length. . . . .	42
5.2	True stress-strain response for subject specific cortical coupon tests conducted in [2]. . . . .	43
5.3	Non time-shifted force-displacement responses. . . . .	44
5.3a	Rib C. . . . .	44
5.3b	Rib G. . . . .	44
5.4	Force-displacement CORA ratings. . . . .	44
5.4a	AHM approach. . . . .	44
5.4b	Difference between AHM and HS approaches. . . . .	44
5.5	Rotation comparison. . . . .	46
5.5a	CORA rotation rating for AHM. . . . .	46
5.5b	Rotation comparison for Rib D. . . . .	46
5.6	Strain gauge-Time history for (a-b) good agreement, (c-d) poor agreement. . . . .	47
5.6a	Rib C posterior strain gauge data. . . . .	47
5.6b	Rib C anterior strain gauge data. . . . .	47
5.6c	Rib A posterior strain gauge data . . . . .	47
5.6d	Rib A anterior strain gauge data . . . . .	47
5.7	Rib B: Comparison of the standard case and the scaled velocity simulation. . . . .	53
5.7a	Force . . . . .	53
5.7b	Anterior Rotation . . . . .	53
5.7c	Posterior Rotation . . . . .	53
5.8	Rib H: Comparison of the standard case and the scaled velocity simulation. . . . .	53
5.8a	Force . . . . .	53
5.8b	Anterior Rotation . . . . .	53
5.8c	Posterior Rotation . . . . .	53

# List of Tables

3.1	Treatment of elements with different aspect ratios . . . . .	20
4.1	Overview of content in modeling approaches. . . . .	27
4.2	Material parameters for support components in simulation setup. . . . .	34
5.1	Mesh quality metrics for all rib specimens. . . . .	40
5.2	Mesh quality shell. . . . .	41
5.3	Mean and standard deviation of CORA rotations rating. . . . .	45
5.4	Mean and standard deviation of the CORA ratings for the strain gauge data. . . . .	47
5.5	Fracture location for post-test experiment (circle) and all undeformed modeling approaches (line). . . . .	49
5.6	Cutaneous view of modeling approaches at experimental fracture time with first principal strain showing. Experimental (circle) and simulation (line) fracture location. . . . .	50
5.7	Cortical thickness distribution of ribs where fracture location was predicted. . . . .	51
5.8	Cortical thickness distribution of ribs where fracture location was inconclusive. . . . .	52
A.1	Energy balance and mass scaling evaluation . . . . .	II





# 1

## Introduction

This chapter presents the background to why this issue should be studied followed by the objective, explaining what is to be investigated, as well as the limitations and the issue under investigation.

### 1.1 Background

The main restraint systems in vehicles today are airbags and seat belts. These restraint systems have significantly reduced the number of occupants killed and injured in automobile crashes. However, when accidents do occur the chest is particularly vulnerable. The most frequent thoracic injury is rib fractures and flail chests. Rib fractures themselves can be life threatening, but can also lead to soft tissue injuries, e.g. hemothorax and pneumothorax, and result in serious complications especially for the elderly population [7].

To design and evaluate occupant restraint systems, a detailed knowledge about the behavior of a human body when loaded in crashes is needed. One of the tools used to predict the risk of injury to an occupant in a vehicle crash is mathematical models of humans, normally called Human Body Models (HBM). With such models, detailed analysis of the behavior of various structures of the body can be evaluated. Output data from a HBM can for example be strain in individual ribs. However, as of today there is a gap between the fracture estimated using HBMs and the actual fractures observed in real car crashes.

To gain a better understanding of the rib cage, an individual rib can be isolated and studied. The major rib response during an automobile frontal crash has been shown to be represented by a controlled anterior-posterior dynamic loading of the rib, allowing for data such as strain, displacement, rotation, moment, forces and fracture location to be recorded [7]. However, attempts to capture the rib fracture in a Finite Element (FE) simulation has not yet been achieved with sufficient precision nor with an adequate set of modelled ribs.

One of the main obstacles in correctly predicting fracture location is believed to be the inability to measure the cortical bone thickness [21, 22]. As of this moment, the best attempt to accurately determine the rib's cortical thickness was extracted from High Resolution clinical Computed Tomography (HRclinCT) that overestimated the cortical area and the area inertial moments  $I_x$  and  $I_y$  with over 100 % [13]. However, Holcombe et al. (2018) have developed a statistical Cortical Bone Mapping (CBM) algorithm that can predict the periosteal and endosteal boundaries of the cortical bone with a promisingly high accuracy. When analysing HRclinCT images with an in-plane 0.373 mm/pixel resolution, the cortical thickness was found within a mean value of  $-0.03$  mm compared to the measurements obtained through micro CT with 0.025 mm/pixel resolution [13].

Consequently, a high precision tool aiming to eliminate one of the potentially largest error sources in the prediction of rib fracture can be deployed. While utilizing an even finer HRclinCT than the one presented in Holcombe et al. (2018) combined with a mapping procedure that will designate rib specific trabecular material data to each rib, prerequisites are in place to successfully present a representative FE model methodology that will predict rib fracture location and thus provides guidelines for further development of the thorax used in impact biomechanic HBMs.

## 1.2 Objective

The objective of this project is to analyze if fracture location and corresponding force can be captured using the first principal strain estimate measured in a single rib FE model utilizing a high resolution clinical CT scan assisted by a statistical mapping method to predict the cortical bone thickness. The FE model is, in an initial approach, to be based on subject specific anatomical data of human ribs and modelled using hexahedral solid elements. Then if the model proves successful in capturing the ribs' structural behaviour, the aim is to reduce the model complexity whilst satisfying the requirement presented in the issue under investigation.

## 1.3 Limitations

This project is limited by the provided experimental data. The experimental data stems from an unpublished study by Dr. Amanda Agnew at Injury Biomechanics Research Center. The geometrical part of the provided data consists of the outer geometry of the ribs with pots obtained through FARO<sup>®</sup> laser scans as well as the highest precision clinical CT scan available (voxel size 0.146 x 0.146 x 0.67 mm/pixel) to determine the cortical thickness distribution. The dynamic response of the ribs are provided through reaction forces, four uni-axial strain gauges and rotations of potting cups with respect to time, from a dynamic anterior-posterior bending test.

Furthermore, the experimental data includes individual cortical material coupon tension tests, taken from the contralateral, un-tested, sixth rib from the same subject.

The purpose of the dynamic loading in the experimental test setup is to mimic the anterior-posterior movement of the rib, pertaining to the major motion of the rib cage during a frontal automobile crash. To make this spine-sternum compression amendable to modeling, the number of degrees of freedom was reduced in an attempt to isolate the response of an individual rib. The simplifications in boundary conditions should be taken into consideration when comparing the results with other studies, as well as with the loading mode experienced by an individual rib inside the thorax.

In this study, the fracture location in the subject specific FE models was defined as the location in which peak first principal strain is measured at the time coinciding with the recorded time for fracture in the experiment. The magnitude of the measured strain at the fracture time in the FE model is not considered, since subject specific data for this validation is unavailable. The prerequisite when applying this methodology is that the FE model response first has been successfully validated against the experimental data to provide sufficient evidence that the experimental response is reproduced by the simulated model without optimization of variables. Once this is established, the probability that the time for fracture in the FE model coincides with the experimental fracture time, is considered high.

## 1.4 Specification of Issue Under Investigation

After completing the thesis, the following hypothesis ought to be confirmed:

- The rib fracture is strain controlled and the cortical bone can be modelled as a continuum using solid or shell elements whilst predicting the rib fracture location and force using the developed methodology.



# 2

## Literature Study

In this chapter, a literature study is presented to provide the reader with insight about the test procedure pertaining to the experimental test as well as earlier findings related to FE rib modeling.

### 2.1 Test Procedure

The test data from the dynamic loading, obtained by the stakeholder for this thesis was provided by Dr. Amanda Agnew<sup>1</sup>. The experimental data stems from an unpublished study performed on the number sixth rib. In a related study conducted by A.Agnew et al. (2015) the exact procedure can be found [1]. The basis for the test procedure was engineered by Charpail et al. (2005) with influences from modifications made by Kindig (2009) [7, 19]. Below, a description of the test procedure used by Agnew et al. (2015) is presented together with notable differences between the test procedures developed by Charpail et al. (2005) and Kindig (2009).

The cortical material data from tension tests on coupons, were taken from the contralateral, un-tested, sixth rib from the same Post Mortem Human Subject (PMHS). The cortical material data was obtained from Virginia Tech as a part of the project conducted by Amanda Agnew [2]. There was a study conducted to quantify the tensile material properties of fractured ribs and compare them to the material properties of contralateral ribs from the same PMHS. It was seen that yield stress and yield strain were significantly different between the fractured and contralateral ribs. However, because of the small sample size and variance within an individual, additional testing was considered necessary [3].

In 2005, Charpail et al. developed a new experimental method to analyze fracture of the human rib. The purpose of the test was to mimic the rib cage motion during frontal car crash, isolating the single rib anterior-posterior movement. The isolated anterior-posterior movement stems from relative motion between the spine and the

---

<sup>1</sup>Ohio State University, Injury Biomechanics Research Center, 2063 Graves Hall,33 3 West 10th Avenue, Columbus, OH 43210, United States

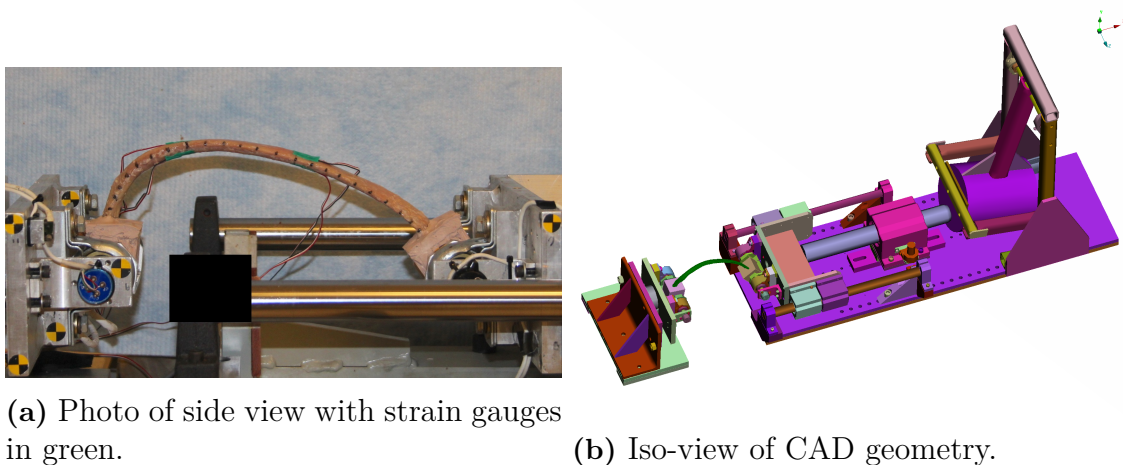
## 2. Literature Study

---

sternum. In order to make the scenario amendable to modeling, the number of degrees of freedom was reduced with focus directed on capturing the major motion of the rib in a spine-sternum compression [7].

From PMHSs, right and left ribs were harvested and removed from the vertebrae and the coastal cartilage. The specimens were abduced of soft tissue and, in a preparation procedure, frozen before being thawed for the ends to be embedded in polyester cement blocks including a hardener. Before fixating the rib in the testing arrangement, four strain gauges were applied. These were positioned at 30 % and 60 % of the curve length of the potted rib, both on the cutaneous and pleural surfaces [1].

The testing arrangement in which the potted ribs were fixated allow for only one degree of freedom at the posterior side. That is, rotation around the rotational axis created by the fixation pin. The anterior extremity was in addition allowed displacement towards the posterior side. The anterior extremity of the rib displace towards the posterior with neither lateral nor superior-inferior offset between the pots [1]. The test setup used by Agnew to produce the data used in thesis is presented in Figure 2.1.



**Figure 2.1:** Test rig used to produce experimental data.

To supply the force needed to displace the anterior end, a 54.4kg mass attached to a pendulum, was set to strike the trolley which the anterior end is connected to. The setup allows force, moments, rotation, displacement and local strains to be measured. The dynamic load was set to reach on average velocity of 1 m/s or 2 m/s [1].

One difference between the test procedures developed by Charpail and modified by Kindig is how the rib is fixated in the testing arrangement. Charpail use cylindrically shaped pots, enclosed by aluminum [7]. Kindig use instead block shaped pots which are screwed together with an U-shaped potting cup (p. cup), made from aluminum [19]. The p. cup used by Kindig is specifically designed so that the the axis of rotation are to pass through both the pot's and p. cup's centre of mass to reduce

the effects of mass moment of inertia about the rotational axis. Charpail however provides no information about the position of the rotational axis in relation to the cylindrical pot. Agnew use a similar, however not identical, p. cup to the one used by Kindig [7, 19, 1].

Kindig thoroughly presents the fixation process of the rib into the testing arrangement. The fixation is performed by adjusting the p. cups while monitoring the read-out from the strain gauges to attempt to find a zero initial strain state. How the fixation process is conducted by Charpail and Agnew is not presented in their articles [7, 19, 1].

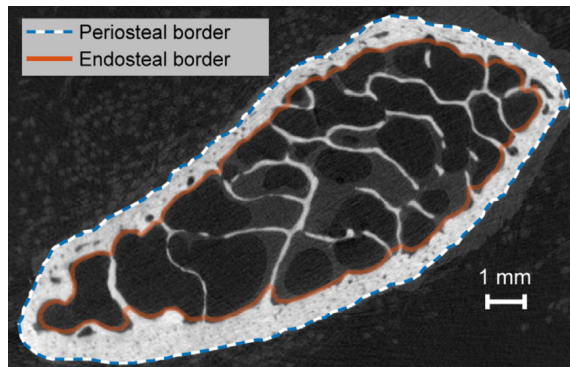
Li have in two separate experiments used a similar setup to the one presented above as a basis for combined quasi-static and dynamic loading [21] and pure dynamic loading [22]. As previously described, rotation around the axis normal to the loading plane was allowed at both extremities of the rib. However, a lateral offset was utilized between the anterior and posterior extremities to account for removed costal cartilage and vertebrae. As a first step in the dual load experiment, a quasi-static loading of 2 mm/s followed by a dynamic loading leading to failure was utilized. In regard to the dynamic load cases, failure occur at either 0.5 m/s or 1 m/s in both cases. The purpose of the experiments was to study FE models for fracture prediction as well as the influence of varying mesh density, cortical thickness and material properties.

## 2.2 Mechanical Properties of Ribs

In this section the geometrical and material aspects affecting the mechanical properties of human ribs are presented.

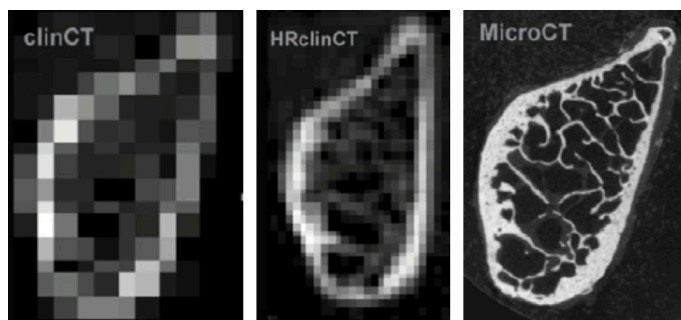
### 2.2.1 Geometrical Properties

Computational models of human ribs are often created based on medical images. Computed Tomography (CT) scans are the most common imaging system used in impact biomechanics to image bones [26]. CT scans utilize the varying tissue opacity to x-rays where the dimensionless Hounsfield Unit (HU) is universally used to determine radiodensity of different tissues, for example the interface between cortical and trabecular bone. This interface is illustrated in Figure 2.2 for a typical high resolution CT scan of a rib.



**Figure 2.2:** Typical microCT with perio- and endosteal borders highlighted. Adopted from Fig.2 in [13].

As is the case with all imaging system, CT scans have a finite resolution which affects the level of detail possible to achieve in the computational model. CT is often divided into clinical CT (clinCT) and micro CT (microCT). ClinCT ranges from low to high in-plane resolution, typically between 0.3–1 mm/pixel. MicroCT has a resolution about 0.02 mm/pixel. A trade-off is that microCT has a narrow field of view and therefore requires small tissue samples only possible to obtain from destructive testing concerning ribs [26]. The difference in resolution between the three levels of detail is presented in Figure 2.3.



**Figure 2.3:** CT images of rib cross section captured with three different levels of resolution. Figure adapted from Fig.4 in [13].

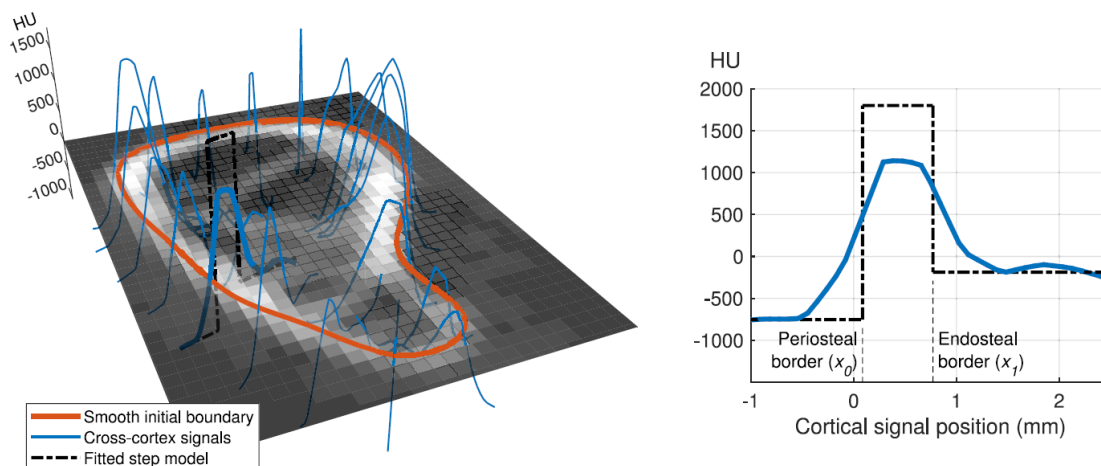
According to Mohr and Kemper the thickness of the cortical bone on a human rib is in the range 0.42–1.22 mm [24, 17]. Consequently, the thickness of the cortical bone is in some areas within the pixel resolution of a clinCT. Thus, the resolution of a clinCT greatly affects the accuracy of the ribs cross-section and therefore also its stiffness when modelled. Perz et al. (2014) concluded in their study that the mean overestimate of the cross-sectional area using HRclinCT was 7.6 %, compared to a greater than 100 % deviation using clinCT, both compared to microCT. It can therefore be concluded that correctly modelling the geometrical properties of the cortical bone is of outmost importance to achieve comparable mechanical properties between the computational model and physical tests.

Results from a study by Holcombe show that their method for determining the thick-



ness of the cortical bone indicate "... substantial reductions in rib cross-sectional measurement error compared to past histogram-based thresholding methods" (p.1 [13]). For example, the method's mean overestimation of the local cortical bone thickness was  $-0.03 \pm 0.17$  mm (mean $\pm$ std) for HRclinCT with 0.373 mm/pixel resolution [13].

The promising results are computed with the help of a Cortical Bone Mapping (CBM) algorithm, developed by Holcombe to process CT scans of bone. The processing is performed by sampling cross-cortex signals across an initial approximation of the periosteal border at multiple locations along the rib, and feed these into the CBM algorithm. By using non-linear optimization, a 6-parameter step model can be fitted to the sampled signals. Outliers are filtered out and remaining is an estimation of the thickness of the cortical bone [13]. The process is also described in Figure 2.4.



**Figure 2.4:** CT image of rib cross-section with initial boundary, sampled cortical signals and the 6-parameter step model fitted. Adopted from Fig.5 in [13].

## 2.2.2 Material Properties

There are several theoretical aspects to the bone's material properties. This is further explained in Section 3.1. Here, focus will be on previously attained findings related to dynamic and quasi-static testing of ribs.

The effect of age is beyond the scope of this study, since subject specific material data will be used. However, worth mentioning is when the single rib is going from subject specific data, to general rib cage for an average representative human body model, the age aspect should not be neglected. Agnew found no correlation between age and fracture location in their experimental study of individual ribs [1]. Though, a correlation between decreasing anterior-posterior displacement pre-fracture with increasing age was detected. Also, ribs not failing during the experiment was located among the lower age specimens. In line with the mentioned findings, the stiffness and

the ultimate stress decrease with increasing age. An increasing brittleness with age was detected which had been established in former studies mentioned in the article. Notable is that a linear model was applied to calculate the structural stiffness, although results indicated nonlinear behavior. Coinciding relations with the study by Agnew was found by Kemper, even though the set of PMHS was remarkably smaller ( $n=6$ ) [1, 18].

Kemper also investigated the effect of sex. The findings state significantly higher average elastic modulus among females ( $p < 0.01$ ). Males were found to have significantly higher average ultimate strain ( $p < 0.01$ ) whereas no significance was found in the difference in average ultimate stress [18].

### 2.3 FE Modeling of Ribs

As of this moment, few attempts have been made to model the rib and validate the results. By studying the attempts made, it can be concluded that capturing the complexity of the rib has been problematic leading to poor results regarding fracture location.

Charpail modelled three of their rib specimens [7]. They were chosen due to their difference in ash density ( $\text{g/cm}^3$ ) and mineral linear density ( $\text{g/m}$ ), extracted from a bone evaluation procedure. The ribs were CT-scanned with slice thickness 1 mm and 0.4 mm resolution perpendicular to the mean line of the natural rib curvature. 4-node shell elements were used to model the cortical bone, with the shell thickness of the average cortical bone thickness among the four nodes. The trabecular bone was modelled by 8-node hexahedral elements. Rigid bodies were used to represent the attachment cap for the rib extremities. Boundary conditions were setup representing the experimental setup. No information was given on the location of the axis of rotation. Cortical bone material data was extracted from the average values gained through the physical test on the sixth and ninth ribs. Material properties used for the trabecular bone was found in literature. Also, failure strain was specified to 10%. Data for comparison is fairly limited due to the small set of modelled ribs. Maximum and minimum strain for two of the ribs where data for comparison existed, corresponded quite well for the time of fracture at the physical test. However, no comparison between experiment and model was made for fracture location. Additionally, the mesh size and quality was not presented nor evaluated.

The two studies from Li, presented in Section 2.1, focused on experiment versus modelling comparisons [21, 22]. Both studies employ rib reconstruction from CT-scans, but the modelling of the ribs and the modelling purpose differs between the studies. One study focused on comparing all hexahedral (all-hex) and combination of shell and hexahedral (shell-hex) elements to experimental data [21]. Here, the triangular surface mesh created from the CT-scan was transferred into a hexahedral mesh. Then, the volumetric mesh was divided into cortical and trabecular

bone using a mask-based material assignment method. The element size ranged from 0.7 to 1.2 mm. In a similar manner, the shell-hex mesh was generated. The shell-hex models were setup with constellations of varying element size and cortical thickness interpretations. The cortical and trabecular bone was assigned the LS-DYNA elastic-plastic material model \*MAT\_03, modified to give failure at a specific plastic failure strain and initiated by element deletion. The required complementary material constants were found in literature. In two out of three cases, the all-hex model managed to predict failure in the correct location. Unfortunately, the shell-hex models were unable to predict correct failure location [21].

In the parallel study of Li, the shell-hex mesh used to model the rib was generated in the same manner [22]. Shell-hex mesh was used for all simulations, with varying constellations of different mesh density and varying/constant cortical thickness. The authors found that it was sufficient to use a model with 3000 hexahedral elements for the trabecular bone and a varying cortical bone thickness to predict the fracture force-failure displacement relationship. Further increasing the mesh density had little effect on this relation. The fracture location was predicted on the sixth rib, where the influence of mesh density and cortical bone thickness had minor effect [22].

Inadequate information was given to determine the location of the axis of rotation in both of the two studies by Li [21, 22]. Nor was information provided on the mass of the pot and whether p. cups were used in the simulation. Another possible drawback in the two studies is the use of an experimental setup incorporating lateral offset between the rib's extremities. This, since incorporating a lateral offset might result in a miss-alignment of the resultant force vector with respect to the translational vector between the rotational axes. Kindig notes that 98% or more of the force measured at the posterior end was directed along the translational vector going through the two rotational axes when utilizing no lateral offset. In comparison, if lateral offset was used, 81% or more of the force was directed along the translational vector [19].



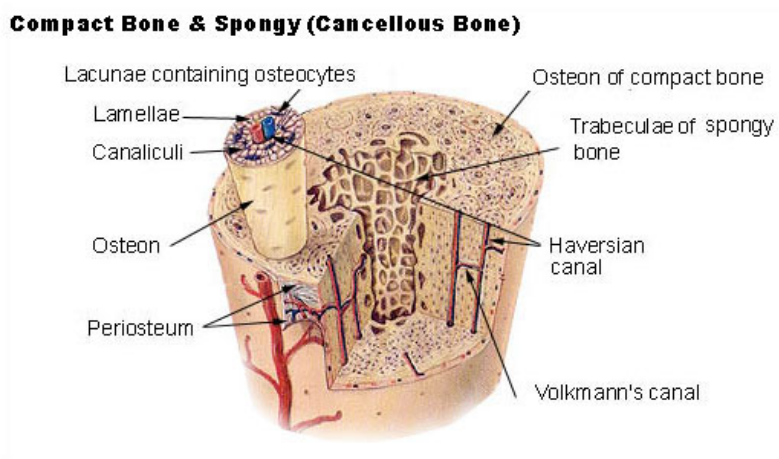
# 3

## Theory

The theory chapter is aimed to introduce technical and medical terms which will be used throughout the thesis, by giving a brief introduction to the structure of bones and the anatomy of human ribs. The chapter also provide some theory involving explicit FEM, element formulations and model assessment.

### 3.1 Microscopic Structure of Bones

Bone is a biological collagen based tissue which amongst other functions serves to give structural support to other tissues. The cross-sectional geometry of bones is optimally designed to give a lightweight construction with the ability to carry high functional loads. The high stiffness, strength and fracture toughness seen in bones are achieved by an inner core of light trabecular bone surrounded by an outer shell of cortical bone, illustrated in Figure 3.1, [12].



**Figure 3.1:** Illustration of a cross-section cut of a long bone. Figure adopted from [32].

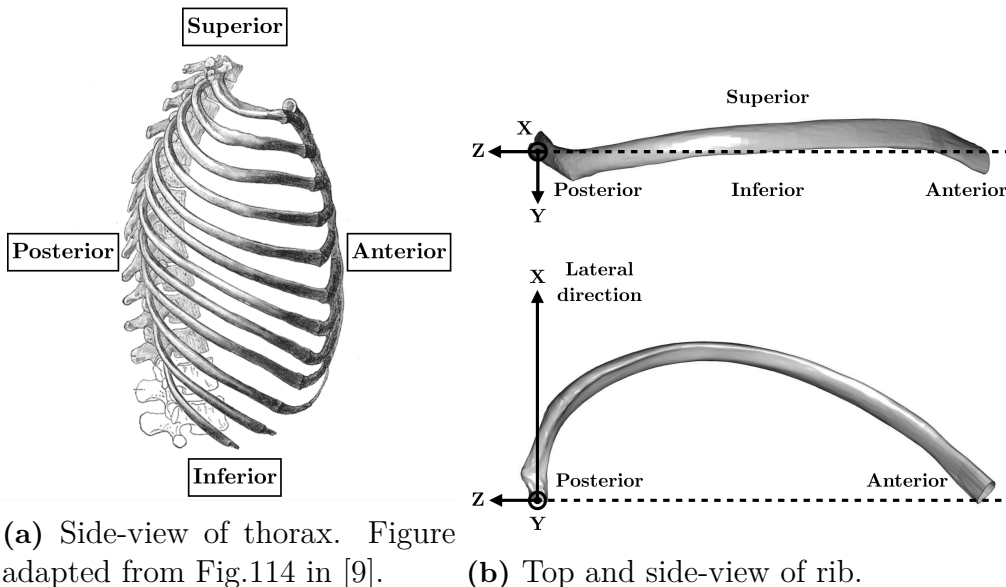
The cortical bone is sometimes referred to as the solid part of the bone. However,

when analyzing its microstructure it is found to be non-homogeneous. The cortical bone consists of a network of repeating functional units called osteons. In long bones, osteons are aligned with the bones long axis. Each osteon has a cross-section where cylindrical layers of lamellae, with different orientation, surrounds the Haversian canal. The Haversian canal houses blood vessels, lymph vessels and nerves. Inside the osteons the Haversian canal branch out to empty spaces named lacunae via channels called canaliculi. The lacunae are occupied by osteocytes (bone cells) enabling communication between cells. The communication between osteons occur via the Volkmann canals which run perpendicular to the Haversian canals [8].

The trabecular bone can be defined as a porous network with a spongy, honeycomb structure. The mechanical properties of the trabecular bone are dependent on the bone volume fraction [8].

### 3.2 Rib Anatomy

The human thorax, seen in Figure 3.2a, serves to protect the organs of circulation and respiration from injury. One of the skeletal components which make up the human thorax are the ribs. The ribs are positioned in the ribcage with an inclination. The inclination is defined as the angle between the thorax's transverse plane and the major plane of the rib. Where the major plane of the rib is the plane described by the origin, lateral most point and z-axis, seen in Figure 3.2b, [9].

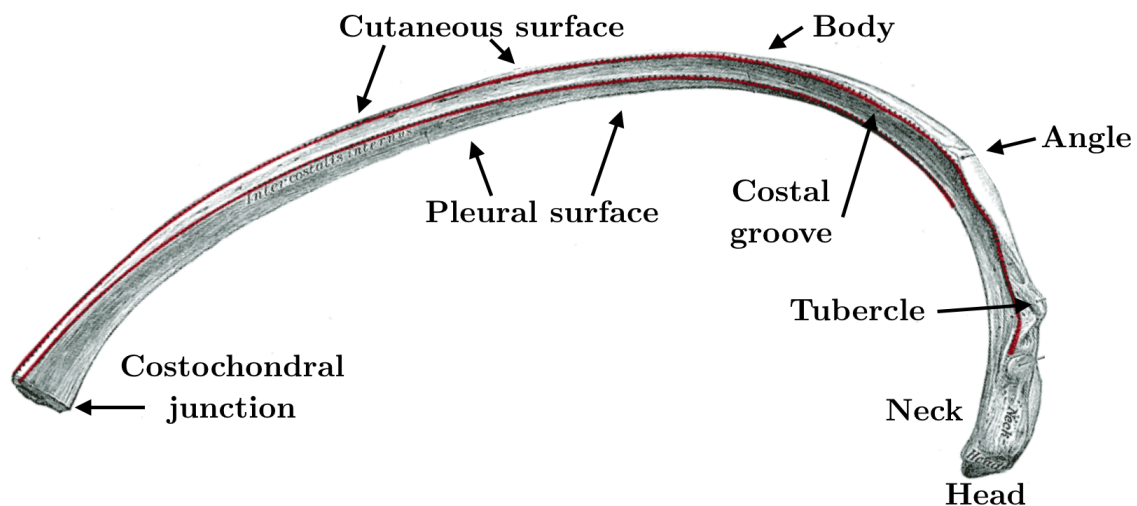


**Figure 3.2:** Anatomical directional terms with a coordinate system used throughout this thesis

The rib cage contains 24 ribs, 12 on either side. The ribs remain in place with posterior and anterior connections. The posteriorly located head and tubercle of the

ribs are connected to the vertebrae, while the anterior connections differ, resulting in a characterizing terminology. The seven most superior located ribs are called true ribs. The true ribs have their individual anterior connection with the sternum via the intervention of costal cartilage. The remaining five ribs are called false ribs. The cartilage of the three superior-most false ribs connect with the cartilage of the seventh, true rib. The two inferior-most ribs, also termed as floating ribs, lack an anterior connection completely. Because of the dissimilar characteristics between the twelve ribs, a rib from the middle is suggested to harvest if the goal is to analyze common characteristics of ribs [9].

If the single rib is studied in more detail several different regions are found. These are highlighted in Figure 3.3. The cutaneous surface is located closest to the skin while the pleural surface face the organs. The angle of the rib, which gives attachment to a tendon, also mark approximately where the costal groove is deepest and broadest. The costal groove is the valley between the inferior boundary and the pleural surface. Finally, the remainder of the rib is called the body [9].



**Figure 3.3:** Rib with structural features. Figure adapted from Fig.122 in [9].

### 3.3 Implicit and Explicit Analysis

The Finite Element Method (FEM) can be used to compute a numerical solution to transient problems described by partial differential equations (PDE). Transient problems with a non-stationary excitation are normally solved by time step schemes. The two main types of time step schemes are implicit and explicit; these are both based on finite differences with respect to time. The implicit approach can solve both dynamic and static problems while the explicit approach requires that there is acceleration present [11].

To highlight the difference between the implicit and explicit schemes, consider the

linear elastic equations of motion on matrix form, see Equation (3.1). Here,  $\mathbf{u}$  represents the displacement,  $\mathbf{M}$ ,  $\mathbf{C}$  and  $\mathbf{K}$  represent the mass, damping and stiffness matrix respectively,  $\mathbf{f}$  is the load, and  $n$  represents the number of discretized time steps  $t \in [t_0, t_0 + \Delta t, t_0 + 2\Delta t, \dots, t_0 + n\Delta t]$ .

$$\mathbf{M}\ddot{\mathbf{u}}^n + \mathbf{C}\dot{\mathbf{u}}^n + \mathbf{K}\mathbf{u}^n = \mathbf{f}^n(t) \quad (3.1)$$

The implicit and explicit approach to Equation (3.1) are seen in Equation (3.2) and (3.3) respectively. Here,  $f()$  denotes a function of.

$$\text{Implicit: } \mathbf{u}^{n+1} = f(\dot{\mathbf{u}}^{n+1}, \ddot{\mathbf{u}}^{n+1}, \mathbf{u}^n, \dot{\mathbf{u}}^n, \ddot{\mathbf{u}}^n, \dots) \quad (3.2)$$

$$\text{Explicit: } \mathbf{u}^{n+1} = f(\mathbf{u}^n, \dot{\mathbf{u}}^n, \ddot{\mathbf{u}}^n, \mathbf{u}^{n-1}, \dot{\mathbf{u}}^{n-1}, \dots) \quad (3.3)$$

It can be noted that the proceeding step,  $\mathbf{u}^{n+1}$ , in the implicit approach depends implicitly on the right-hand side of Equation (3.2). Hence, at least one iteration is needed to establish equilibrium of the internal structure forces with the externally applied loads. Conversely, the proceeding step in the explicit approach depends solely on known terms, meaning that it can be solved for explicitly.

The disadvantage of the implicit solver is that it requires computationally costly matrix inversion. However, the solver has no inherent limit on the size of the time step. The implicit solver therefore requires relatively few but expensive time steps. Although, for nonlinear problems including contact and material nonlinearities, the implicit solver requires a smaller time/load steps depending on the convergence behaviour to obtain equilibrium [11].

The advantage of the explicit solver is that the equation for the proceeding time step can be solved for directly. However, the maximum time step is limited by the Courant-Friedrichs-Lewy (CFL) condition. Hence, the explicit solver is only conditionally stable. The explicit solver therefore requires many, relatively inexpensive time steps. As a consequence it handles nonlinearities with relative ease compared with the implicit solver [11].

### 3.3.1 The Courant-Friedrichs-Lewy (CFL) Condition

The CFL condition is the constraint explicit schemes must satisfy to ensure stability. This enables the solution of a difference equation to converge. In order for the CFL condition to be satisfied, all necessary information in the initial data must be used by the difference scheme. de Moura and Kubrusly (2013) use the following elaboration [25].



*To satisfy this condition, the ratio of the spatial discretization to the time discretization must be at least as large as the largest velocity with which signals propagate in solutions of the partial differential equation. This inequality is called the CFL condition.* [25]

Thus, the CFL condition results in an upper boundary on the time step,  $\Delta t_{\min}$ . In this project, the upper boundary i.e. the critical time step corresponds to the time it takes for a sound wave to travel across an element. The wave propagation velocity in 3D-continuum,  $c_{3D}$ , is applied. It is known from Equation (3.4) [11].

$$c_{3D} = \sqrt{\frac{E(1-\nu)}{(1+\nu)(1-2\nu)\rho}} \quad (3.4)$$

$$\Delta t_{\min} \leq \frac{l}{c_{3D}} \quad (3.5)$$

From Equation (3.5) it can be concluded that small elements,  $l$ , high stiffness,  $E$ , and low density,  $\rho$ , reduce the critical time step resulting in a higher CPU demand.

### 3.4 Mass and Time Step Scaling

As the CFL condition regulates the time step, mass scaling is an alternative to manipulate this condition to achieve reduced simulation time. Equations (3.4) and (3.5) declares that an increase in density will result in a longer critical time step. By adding mass to the element, this is achieved. In LS-DYNA, this procedure is determined in `*CONTROL_TIMESTEP` when invoking `DT2MS`. If a negative value of `DT2MS` is stated, a nonphysical mass is added to elements whose time step surpasses this value. Though, as mass is added to the system, the dynamic equilibrium is altered (recall  $F = ma$ ). Hence, it is necessary to evaluate its significance in the solution. Engineering guidelines exists on permitted increase of mass, but in the end, it is case dependent.

If stability is an issue, the time step can be further altered by scaling the CFL condition. For stability reasons, the scale factor, selected in `TSSFAC`, is 0.9 by default in `*CONTROL_TIMESTEP`. If mass scaling is activated, the time step is defined by  $TSSFAC \times DT2MS$ .

## 3.5 Solid Hexahedral Elements

When large curvature is present and through-the-thickness strain is of interest, traditional thin shell elements are not recommended to use in FE analysis. Instead solid elements are preferred. When using solid elements, especially in dynamic simulations, the hexahedral elements are in general considered to be both more accurate and efficient compared with tetrahedral elements. Burkhart et al. (2013) suggest using hexahedral elements for meshing biological structures in dynamic scenarios because of their superiority over tetrahedrals in terms of accuracy, stability and insensitivity in mesh refinement [6, 11].

In LS-DYNA, the eight-node hexahedral solid element is probably the most used element. The eight-node hexahedral element is most frequently used with single-point integration combined with an hourglass (HG) control. A desired benefit of using single-point integration is the reduced computational cost. However, the accuracy of the numerical integration is more exact when using full integration compared with reduced integration. If reduced integration can be justified or not is case dependent. Reduced integration is recommended to increase robustness for large deformations and to avoid locking phenomena in problems involving constant volume bending modes where the behaviour of the material becomes incompressible [11].

## 3.6 Shell Elements

Going from theory of solids to shell theory, two or in some cases three rotational degrees of freedom are added to the already existing three translational degrees of freedom. This governs that all shells can experience bending, membrane and shear deformations. Though, the possibility to capture the out-of-plane shear deformations is reduced with the Love-Kirchhoff assumptions that state (a) plane cross sections remain plane during deformations and (b) normal stresses to the middle surfaces are negligible. This governs a constant through-the-thickness shear strain [14, 20]. Two states of deformation define the behaviour of shell elements, namely membrane and bending deformation. Shells possess higher stiffness in membrane direction. Hence, to make full use of a shell structure, the structure should be adapted to have the load acting in membrane direction [5].

### 3.6.1 Thick Shells

Thick shells are layered eight-noded elements with four nodes defining the top and bottom surface individually. Theory wise, they undertake the theory of shells with the option of adding an assumed strain expressing the general theory to comply with the 3D stress state found in solids. LS-DYNA offers four different element

formulations for thick shells. Element formulation 1 and 2 yields a stress state found in pure shell theory and offers no advantages over thin shells. In element formulation 3, the addition of the 3D stress state is found, but its usage in explicit simulations are redundant. However, element formulation 5 offers a 3D stress state with a shear locking and hourglass stabilization, due to the assumed strain method, and it can be used with only one element over the thickness [29, 11].

Nevertheless, stability problems are often found in simulations using thick shells and it lies to a certain extent in the choice of solver version. Due to thick shells being used increasingly, enhancements are made progressively and therefore a later version of the solver is often preferred. Attention in the development of the thick shells is mainly compliance with composite modelling [15].

### 3.6.2 Thin Shells

The thin shell is a 2D element formulation that operate under the assumption of plane stress. Thin shells can be fully integrated or employ reduced integration with the addition of hourglass control. In LS-DYNA, element formulations 2 and 16 are the only recommended shells for the general application. Element formulation 2 has one in-plane integration point element and efficiency is its main argument. However, problems can occur in cases of large shear deformations. Utilizing element formulation 16 provides a fully integrated element with no necessity of hourglass control. Though, hourglass control 8 can be added to improve warping behaviour. Since it is fully integrated, the locking phenomena can occur which may stiffen the response. The formulation is considered accurate with the computational cost as a drawback [29].

The number of integration points through-the-thickness must be compliant with the intended application. For pure membrane action, one integration point is sufficient as no bending actions needs to be resisted. Handling nonlinear materials, at least three to five integration points are recommended. LS-DYNA offers the option of Gaussian or Lobatto integration where the Gaussian integration is regarded as the preferred choice in terms of accuracy. [29, 11]. As most thin shells are based on the assumption of constant transverse shear strains, a violation of the condition of zero traction on the shell surfaces occurs. In an attempt to correct this violation, a shear correction factor is applied with the recommended value of  $5/6$  [11].

## 3.7 Hourglass Control

A disadvantage which arises from reduced integration is the introduction of zero energy modes also referred to as HG modes. Hourglassing occurs when an element becomes distorted without strain energy being generated. The element can deform

without the presence of strain energy because it has no stiffness in the deformation mode [4].

So called HG control is introduced to counteract HG modes. HG control introduces internal nodal forces which resist the HG modes. The internal forces can either be proportional to components of nodal velocity or nodal displacement, where the respective names of these two types of HG controls are viscous based and stiffness based. Briefly, viscous based control is often used for high velocity simulations while stiffness based is used for low velocity [11].

The 3D Patch Test is a method used to evaluate how well an HG method represents a constant stress/strain field. In an assessment, using the 3D patch test by Schwer et al. (2005), of HG control applicable to solid elements in LS-DYNA it was concluded that only three out of six managed to confirm the analytical stress results. The HG controls, specified by IHQ in keyword \*HOURLASS, recommended by the authors, were the viscous based control number 3 or the two stiffness based controls 5 and 6 [28]. Therefore, depending on the amount of HG deformations and HG energy, choosing the correct HG control can affect the accuracy of the results.

### 3.8 Mesh Quality

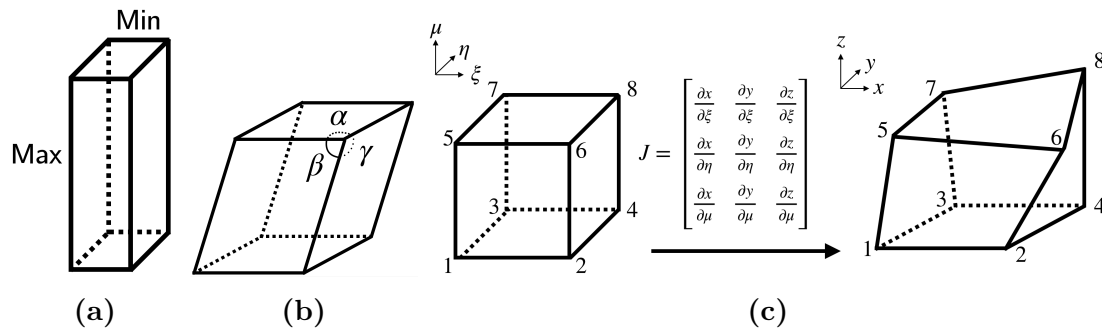
Mesh quality is a potential source of error when modeling a physical system described by partial differential equations using the finite element method. It is of importance to quantify the mesh quality in order to control the affect a mesh has on both the accuracy of the solution and the efficiency of the simulation.

Distorted elements often occur in FE meshes of biological structures such as human ribs as a consequence of the complex geometry. Burkhart et al. (2013) presented a study in which recommendations are given for specific quality criteria to be used when assessing mesh quality in FE models representing bone tissue [6]. The quality criteria includes three different metrics: aspect ratio (AR), angle idealization and Jacobian. The definitions are presented below and are illustrated in Figure 3.4.

The AR of a hexahedral element is calculated by dividing the length of the longest edge by the length of the shortest edge. The most accurate elements have an AR equal to 1. In Table 3.1 the categorization of ARs is given. The user should aim to have less than 5 % of the elements exhibit an  $AR > 3$ .

**Table 3.1:** Treatment of elements with different aspect ratios

Aspect ratio	Mark
$1 < AR < 3$	Acceptable
$3 < AR < 10$	Treat with caution
$AR > 10$	Treat with alarm



**Figure 3.4:** Illustration of the mesh quality metrics; (a) aspect ratio, (b) angle idealization, and (c) Jacobian

The angle idealization of a hexahedral element infers that the interior angles should not deviate too much from the ideal  $90^\circ$ . The angle idealization considers the 24 angle measurements located at the eight vertices of an hexahedral element. Here, the internal angle measurement should exhibit an absolute deviation exceeding  $70^\circ$  in less than 5% of the elements.

The Jacobian of an element refers to the determinant of the Jacobian matrix and is a measurement of the volume distortion. The Jacobian represents the transformation from an ideal unit cube in the parent domain to the actual element in the global domain. Thus, a Jacobian equal to 1 represents a perfectly shaped element.

The criterion for mesh quality in terms of the Jacobian is divided into three subcriteria; (a) Jacobians should have a positive value, (b) The Jacobian should preferably be greater than 0.2, (c) less than 5% of elements should have a Jacobian greater than or equal to 0.7

### 3.9 Energy Balance

When modeling systems using FE simulations it is of importance to ensure that the numerical results are obeying the law of conservation of energy. To ensure this, it is strongly recommended that the models global energy is checked by studying the energy balance for inconsistencies. An example of an inconsistency that should be monitored is the hourglass energy [6].

In LS-DYNA, the global energy balance is assessed by monitoring the energy ratio. The energy balance is considered perfect if the energy ratio between the total energy  $E_{\text{tot}}$  divided by the initial energy  $E_{\text{tot}}^0 + W_{\text{ext}}$ , is equal to 1.0. The total energy consists of the current kinetic energy, initial energy, and possibly sliding interface energy, rigid wall energy, damping energy, and hourglass energy. The initial energy consists of initial kinetic energy, initial internal energy and external work [16]. In this project the energy ratio can be simplified to Equation (3.6) since there exist

no initial kinetic energy, nor any initial internal energy. Thus, the energy ratio represents a balance between the total energy  $E_{\text{tot}}$  consisting of the current initial, kinetic and hourglass energy, and the external work  $W_{\text{ext}}$ .

$$\text{Energy ratio} = \frac{E_{\text{tot}}}{W_{\text{ext}}} \quad (3.6)$$

If the energy ratio constraint is not fulfilled, there might be an error in the results. The ratio can deviate in two ways; either by the energy ratio being greater than 1.0, indicating that energy is being introduced artificially, from for example numerical instabilities. Or if the ratio falls below 1.0, indicating that energy is being absorbed artificially, for example by excessive hourglassing [16].

Burkhart et al. (2013) suggest that an acceptable deviation for the energy ratio is  $\pm 5\%$ . Also, if an HG control is implemented to control the hourglass energy, an analysis should be conducted to ensure that the HG control did not contribute with more than 10% of the total energy [6].

# 4

## Materials and Methods

All of the model build up described in this chapter, if not stated otherwise, were performed using the pre-processor ANSA v18.1.2 of BETA CAE Systems.

First to be presented in this chapter is the material used in the validation of the simulations. Second in this chapter is the solver controls and the curve-to-curve comparison procedure. Third is an overview of how the simplification process was conducted starting from the most detailed approach. Following the overview are in-depth sections describing the different procedures involved in the steps touched upon in the overview.

### 4.1 Experimental Data for Validation

The experimental data obtained from the test procedure described in Section 2.1 was used to validate the behavior and accuracy of the implemented FE models.

The test data used as validation was taken from a spreadsheet provided to the project by the stakeholder. It contains the data presented in the list with respect to time.

1. Force in the main loading direction, corresponding to the z-direction, measured by the load cell located at the posterior side.
2. Rotations of the p. cups measured by rotational potentiometers.
3. Displacement in the z-direction of the anterior support components measured by a linear string potentiometer.
4. Acceleration for the anterior support components measured by accelerometers on the anterior support components.
5. Uni-axial strains in longitudinal direction measured by four strain gauges po-

sitioned on the pleural and cutaneous surfaces at 30 % and 60 % of the curve length of the potted rib.

By default, the data acquisition system considers the start of data collection as time  $t_0 = 0$ . As a consequence, the time  $t_1$  when the specimen actually began to experience a build up of force, defined as the start time in the spreadsheet, is not at time zero,  $t_1 > t_0$ . The implication of this is twofold. First, the definition of time zero is not directly transformed to the simulation results. Second, all experimental data is corrected so that the measured values are zero at  $t_1$ . All experimental data in this thesis are only presented from the time equivalent to  $t_1$  up to the time defined as the fracture time in the experiments.

## 4.2 Curve-to-curve Comparison

It is of interest to calculate and quantify the level of correlation between time-history signals computed from numerical simulations with time-history signals extracted from physical tests. To enable such an objective comparison, the CORelation and Analysis software CORA 3.6 (PDB , Gaimersheim, Germany) was used.

### 4.2.1 CORA

The proposed settings for CORA comparison, documented in the CORA manual, was used with the exception for the interval of evaluation (IOE) and the phase shift [31]. The reason for altering these two settings are given below.

The results from each simulation was compared with only one test. Despite this, the default combination, involving both the corridor and cross correlation method, were used to perform the curve-to-curve comparisons. By including both metrics, the respective disadvantages of each method are compensated for, as intended by the CORA developers [31].

The default constant width method was applied to determine the width of the inner and outer corridor used in the corridor method. This pertains to inner and outer corridors of 5 % and 50 % of the peak value, respectively. The rating from the corridor method ranges from poor to good, equivalently 0 to 1, with a quadratic decline [31].

The cross correlation method in CORA ranks the match between a reference curve and a comparison curve from 0 to 1. The ranking is performed by separating the characteristics of the signal into three analyses; phase shift, size and progression. Before these three quantification values are computed, multiple time-shifts are performed by moving the reference curve within the IOE. The time-shift, corresponding



to the maximum cross correlation value, is then used to compute the three quantification values. Lastly, individual weighting factors are applied to the three values which are then summed up to the total cross correlation rank. The default weighting factors are 0.25, 0.25, 0.5 for the phase shift, size and progression, respectively. Since the signals investigated in this project lack a sufficiently large waveform to accurately make use of the phase shift quantification, it was seen as more logical to set the phase shift weight factor to zero and keep the weighting ratio between the size and progression. This results in the following weighting factors 0, 1/3, 2/3 for the phase shift, size and progression, respectively [31].

With the use of individual weighting factors, the results from the corridor and cross correlation method were summed up to an objectively quantifiable measurement. Here, a default weight factor of 0.5 was used for both metrics.

Before the numerical results were processed in CORA they were resampled to the same sampling rate with respect to time, used in the experiments. The resampling was performed with MATLAB (The Mathworks, Natick, MA), and the function `interp1.m`. In addition, the noisy strain gauge data, recorded in the experiment, was filtered in MATLAB using a SAE J211 recommended four-pole phaseless 60 Hz lowpass filter [10].

For all numerical results compared in CORA, the IOE was decided to start at 5% and end at 90% of the experimentally measured fracture time. The IOE start time is a consequence of the uncertainty pertaining to the start time of the experiment. The IOE end time is shortened because of oscillations seen in the experimental data at the experimental fracture time. Since the overall curve-to-curve comparison is of interest, the IOE settings are considered reasonable.

The intended use of the CORA evaluation is solely to allow for an objective relative comparison between data, used or computed, in this project. Therefore, the difference between CORA ranks is of interest, not their absolute value. As a consequence, the absolute CORA ranks should not be used as a rating of the models biofidelity.

### 4.2.2 Paired t-test

To allow for comparisons between modeling approaches, the paired t-test was seen as a suitable statistical procedure to determine whether the mean difference between two sets of observations, for example anterior rotation, is statistically significant.

The following assumptions are considered to be fulfilled in the cases for which a t-test was employed.

- The dependent variable is continuous (in an interval).

- The observations in the sets are independent of each other.
- Outliers are not included in the dependent variable.
- The dependent variable is approximately normally distributed.

As seems to be the case with a lot of real-world data, the assumption of normal distribution is not straight forward to show with smaller samples. Therefore, the assumption is considered to be met if the dependent variable seems to have a symmetrical shape, with a bell-shape tendency.

### 4.3 Fracture Location Metric

It was of interest to introduce a fracture location metric to assist a visual comparison of the fracture location when determining if the numerical model has captured the accurate fracture location seen in the experiment.

The position for the fracture in relation to the strain gauges was recorded in the provided experimental data. It should be mentioned that both the locations of the strain gauges as well as the relative measurements from the gauges to the fracture locations were measured using a soft tape measure along the rib. The rib in turn, is very irregular in shape. Therefore, all measurements probably contain some unquantifiable error, resulting in that the fracture location metric is recommended to be used in combination with a visual inspection.

The proposed fracture location metric is presented in Equation (4.1). It takes the absolute difference between the experimentally recorded fracture location and the location of the element with the peak first principal strain at the experimental fracture time, along the cutaneous curve. Since the rupture of the rib is initiated in tension, all measurements are taken on the cutaneous side [7]. Because the ribs are of varying length, the absolute difference is divided by the cutaneous curve length measured between the two pots.

$$\text{Fracture location metric} = \frac{|\text{Fracture pos. Exp} - \text{Fracture pos. Sim}|}{\text{Curve length}} \quad [\%] \quad (4.1)$$

Fracture is determined to have been captured if the fracture location metric is less or equal to 15 %.

## 4.4 Solver Controls

The LS-DYNA (LSTC, Livermore, CA) solver version 9.2 with single precision and MPP scalability was used to compute the results presented in this Thesis.

Large deformation theory was applied because of the dynamic anterior-posterior loading condition and consequent large deformations of the highly-curved sections of the rib specimens [19]. Thus, strains in the model are evaluated based on the finite strain theory. Green-St. Venant, or equivalently Green-Lagrangian, strains were used with the stress defined as the second Piola-Kirchhoff stress.

## 4.5 Simplification Process

The strategy to accomplish the objective presented in Section 1.2 was to start by employing the most detailed modeling approach followed by a gradual simplification until the fracture location no longer could be predicted. The different modeling strategies investigated are presented in Table 4.1.

**Table 4.1:** Overview of content in modeling approaches.

Modeling approach abbreviation		<b>AHM</b>	<b>AHV</b>	<b>TSA</b>	<b>SA</b>
Cortical representation	Type	Solid	Solid	TShell	Shell
	ELFORM	1	1	5	16
Trabecular representation	Type	Solid	Solid	Solid	Solid
	ELFORM	1	1	1	1
Homogenized trabecular		No	Yes	No	No
Hourglass control IHQ	Solid	5	5	5	5
	Shell	N/A	N/A	N/A	8

### 4.5.1 AHM - All-Hex Map approach

The most detailed approach to model the subject specific ribs used an all hexahedral mesh to represent the trabecular and cortical bone. Three elements through-the-thickness was used in the cortical bone to resolve the through-the-thickness stress and strain distributions. The material properties for the trabecular bone was mapped from the tetrahedral mesh provided by Maida [23]. The element size was chosen with regards to the lower bound set by the triangulated surfaces generated with the CBM method and to provide mesh metrics complying with the mesh quality criteria presented in Section 3.8. This approach is referred to as *AHM - All-Hex Map* approach.

### 4.5.2 AHV - All-Hex Voigt approach

The first simplification made to the modeling was done to the material properties of the trabecular bone. Otherwise, the same settings were used as for the AHM approach. The subject specific material properties of the multi-property trabecular bone, provided by Maida, was homogenized into one linear elastic isotropic material with a single, homogenized material property for the Young's modulus and mass density [23]. This approach is referred to as *AHV - All-Hex Voigt* approach.

### 4.5.3 HTS - Hex Thick Shell approach

The second simplification made was to represent the cortical bone with thick shells instead of solids. The trabecular bone was still modeled using the multi-property map. This approach is referred to as *HTS - Hex Thick Shell* approach.

### 4.5.4 HS - Hex Shell approach

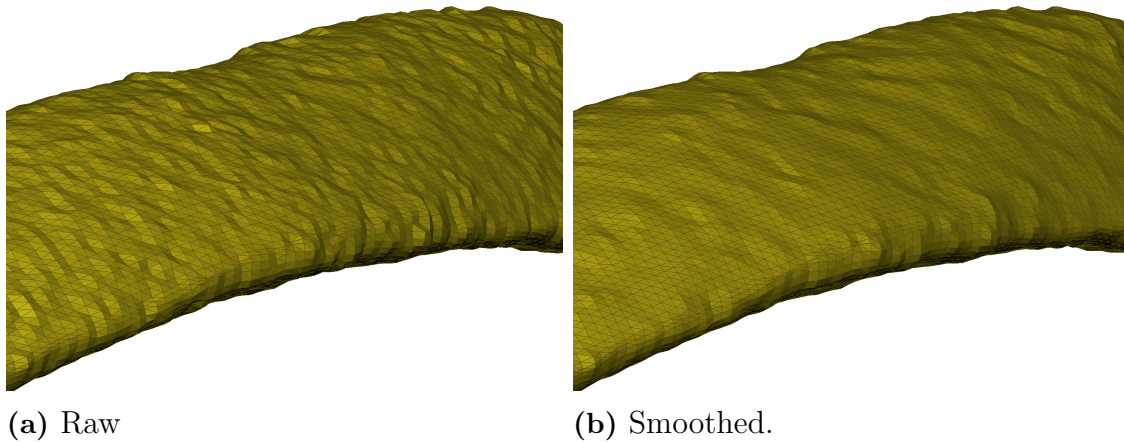
In the third simplification the cortical bone was modeled using thin shell elements while modeling the trabecular bone using the multi-property map. This approach is referred to as *HS - Hex Shell* approach.

## 4.6 Hexahedral Meshing Procedure

The hexahedral mesh representing the trabecular and cortical bone was constructed based on the triangulated periosteal and endosteal surfaces of the cortical bone generated by the CBM method, see Section 2.2.1. The voxel size in the HRclinCT images processed with the CBM method is  $0.146 \times 0.146 \times 0.67$  mm/pixel.

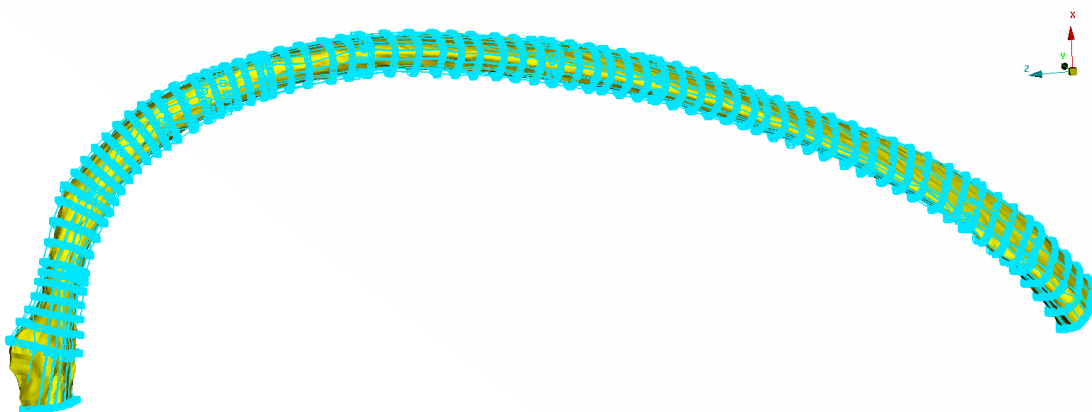
The two surfaces of the cortical bone were visually inspected to determine if the amount of bumpiness on the surfaces required smoothing procedures in order to obtain a meshable surface. Overall, the periosteal surfaces were relatively smooth and therefore required minimum to no smoothing. Conversely, the endosteal surfaces exhibit bumpiness which originates both from connections with trabecular arms as well as from anomalies and outliers in the CBM method. Therefore, engineering judgment was used when reducing the bumpiness to avoid smoothing out natural bumps while still obtaining a meshable surface describing the nature of the endosteal surface. In Figure 4.1 the raw and smoothed endosteal surfaces of rib specimen Rib H can be seen. The smoothing was performed using the *Suppress>Noise* command

in ANSA Pre-processor with the intensity factor set to *local peaks (ultra low)*, *Move only nodes*. These settings minimized shrinking of the volume.



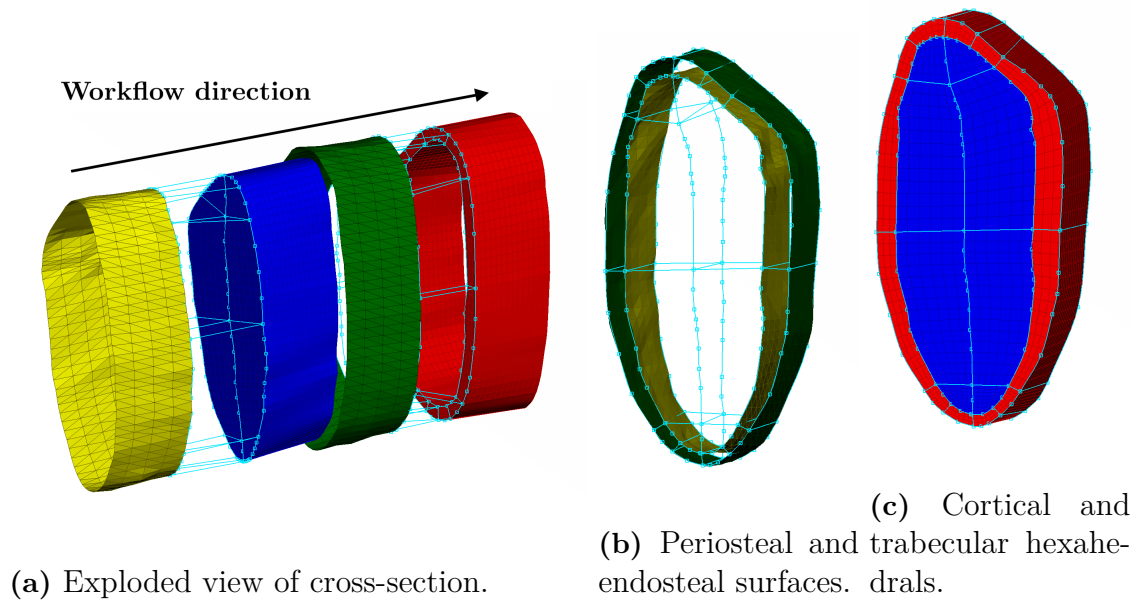
**Figure 4.1:** Raw and smoothed versions of the endosteal surface of rib specimen H.

After discussions with the team at BETA CAE Systems, a semi-automatic Hexa-Block meshing procedure was found to be the best approach to discretize the highly complex and irregular geometry of human ribs. Hexa-Boxes were created and projected to the endosteal surface. With the Hexa-Boxes fitted, the boxes were segmented sufficiently many times to capture the varying geometry along the length of the rib. The segmentations was followed by a projection of the resulting cross-sectional edges to the underlying endosteal surface. Once fitted, the end-points of the boxes were slid along the cross-sectional edge to obtain the best possible square shape for that cross-section taking into consideration the neighboring boxes. The endosteal surface of rib specimen H with Hexa-Blocks fitted is seen in Figure 4.2.



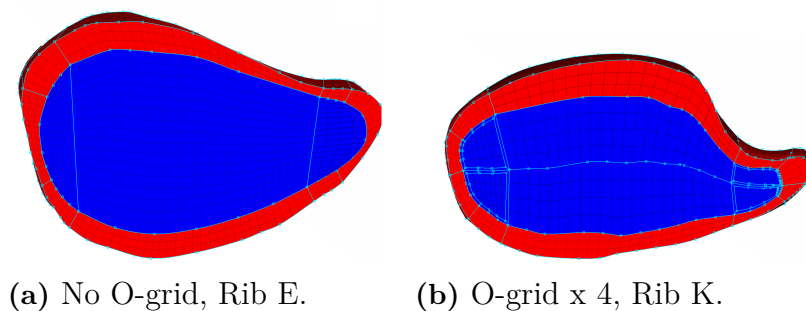
**Figure 4.2:** Endosteal surface with Hexa-Boxes fitted.

The two first rib specimens to be meshed used O-grids in the trabecular mesh. A comparison is seen in Figure 4.4. O-grids were the first meshing method tested which



**Figure 4.3:** Illustration of how the hexahedral mesh is created, yellow=endosteal surface, blue=trabecular solids, green=periosteal surface, red=cortical solids, light blue=Hexa-Boxes.

yielded a mesh enabling simulations to be run. As the meshing procedure developed with each rib specimen it was found that the O-grid generated worse quality meshes than not using it. With the trabecular bone fully boxed in by the Hexa-Boxes, the



**Figure 4.4:** Resulting mesh without and with the use of O-grid.

outer faces of the Hexa-Boxes were offset outwards in their normal direction followed by a fitting to the periosteal surface. With both the trabecular and cortical bone encapsulated by Hexa-Boxes, a mesh of pure hexahedrals was created in the volumes represented by the boxes, as illustrated in Figure 4.3.

The CBM method provides the endosteal and periosteal surfaces with a resolution of  $300 \times 80$  (length  $\times$  circumferential) based on underlying HRclinCT with a resolution of  $0.146 \times 0.146 \times 0.67$ . This grid size sets an upper limit on the available information in terms of overall geometry and cortical thickness. The element size in lengthwise and circumferential directions were explicitly defined for each rib specimen individually. This, to ensure that mesh density is sufficiently large to capture

the underlying detailed geometry while still providing mesh quality metrics in line with the requirements stated in Section 3.8. It can be noted that using three elements through-the-thickness in the cortical bone significantly decrease the feasible element length in the lengthwise direction to ensure elements with an acceptable aspect ratio.

With the cortical bone meshed a membrane was created sharing the nodes with the outermost surface of the cortical hexahedrals. The membrane used ELFORM 5 which corresponds to a Belytschko-Tsay membrane. It was given a minimized finite stiffness, thickness, Young's modulus, and one integration point through-the-thickness in order to measure the strains at the surface without affecting the physics. Four elements on the membrane coinciding with the measured positions of the four strain gauges were assigned to output strain history.

## 4.7 Thick Shell Generation

Starting from the end product of the all-hex mapped setup, the solid element representation of the cortical bone was converted into a thick shell. Owing to the current solid representation, it must in a first step be remapped as it is represented using three elements through-the-thickness and containing a material orientation generating a disoriented thick shell. Utilizing the ANSA function *Vol.skin* on the cortical property, a quadrilateral surface mesh was created. Through the function *Structured Mesh>Map*, a new solid property was mapped between endosteal (*master*) and periosteal (*slave*) surfaces of the mesh while allowing for change in the *Round area* granting one solid element through-the-thickness. In a final step, the solid to thick shell conversion was generated with the LS-DYNA function *Element>Util>Change Type>3-D Entities*. The thick shell was designated ELFORM 5 with three through-shell-thickness integration points. Material properties were transferred from the previous cortical solid element representation.

## 4.8 Thin Shell Generation

Having the thick shell representation accessible, the function *Element>Shell>By Thick Shell* converted the thick shell into a thin shell. In the conversion, the nodal thickness was preserved as well as the material properties. From the procedure of offsetting the thin shell to the middle surface, a void was created between the newly created thin shell and the trabecular solid element representation. To fill this void, a similar mapping procedure, as in Section 4.7, between the thin shell and outer trabecular surface was applied. However, since the thin shells possess the nodal thickness, there will be a thickness overlap with this approach and the void will be "double filled". The elements filling the previous void were assigned identical

properties to the trabecular solid elements they were mapped from. The property designation is further described in Section 4.9. The thin shell was assigned ELFORM 16 with shear correction factor  $5/6$ , three through-shell-thickness integration points and hourglass control 8.

### 4.9 Mapping of Trabecular Material Properties

In Section 3.1, the trabecular bone is described as a porous network with a spongy, honeycomb structure, where the mechanical properties are dependent on the bone volume fraction. An attempt to model this structure was made in a Master's Thesis by Maida (2017) [23], conducted on the same set of ribs used in the present study.

Subject specific, tetrahedral meshes of the trabecular bone, each with 20 different linear elastic material properties, was produced by Maida (2017) with the help of the 3D Image Segmentation and Processing Software Simpleware ScanIP (Synopsys®, Inc.). Default values found in Simpleware ScanIP was applied for the mesh generation, to determine the relationship between the Hounsfield unit, mass density, and Young's modulus.

A python mapping algorithm called *MapSolids.py* was developed in order to transfer the material properties from the tetrahedral mesh to a hexahedral mesh. By defining a search distance, source and target properties, the SGRAPH functionality in ANSA Pre-Processor locates the nearest source-target match and assigns the properties of the source element to the target element. Unmatched elements are placed in a separate set to allow for a subsequent manual match.

### 4.10 Homogenization of Trabecular Material Properties

There exists different a priori methods to obtain the effective material properties of a heterogeneous material consisting of different solid phases. Perhaps one of the more accurate methods, if feasible, is to determine the effective stiffness by imposing unit strains on a FE model of a representative volume element (RVE). However, to represent the tetrahedral mesh provided by Maida (2017) [23], with a RVE was considered too involved. This, since a RVE both needs to be sufficiently small to satisfy the scale separation condition as well as sufficiently large so that averaged field variables do not change if the size of the RVE was increased [27].

The homogenization of the linear material properties representing the tetrahedral based trabecular bone was carried out using the Voigt assumption. The Voigt as-



sumption can be described as a weighted mean which gives the upper bound of the homogenized mass density and elastic stiffness [27].

The Voigt assumption  $\bar{E}^{\text{Voigt}}$  and  $\bar{\rho}^{\text{Voigt}}$  for a material with two phases is computed using Eq (4.2) where  $E$  is the Young's modulus,  $\rho$  is the density,  $n$  is the number of phases,  $v$  is the volume, and  $w$  is the mass.

$$\begin{aligned}\bar{E}^{\text{Voigt}} &= \sum_{i=1}^n \left( E_i v_i \sum_{j=1}^n \frac{1}{v_j} \right) \\ \bar{\rho}^{\text{Voigt}} &= \sum_{i=1}^n \left( \rho_i w_i \sum_{j=1}^n \frac{1}{w_j} \right)\end{aligned}\tag{4.2}$$

The actual value of the homogenized material property is not of interest in this project since the aim of a homogenization of the material properties of the trabecular bone solely is to investigate if the simplification of using a single material property is valid.

## 4.11 Cortical Material Data Processing

The material properties for the cortical bone used in the simulations are taken from subject specific, uni-axial tension tests on material coupons extracted from the contralateral rib from the same PMHS. The tests were performed with a strain rate of approximately 0.5 1/s. The subject specific data provided consists of Young's modulus and engineering stress versus engineering strain curves for all rib specimens [2].

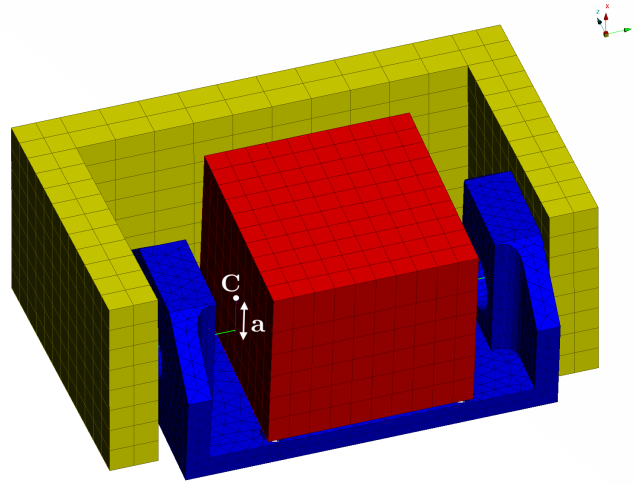
The elasto-plastic LS-DYNA material model MAT\_PIECEWISE\_LINEAR\_PLASTICITY (\*MAT\_024) was used together with a load curve representing the true stress versus true effective plastic strain for the cortical bone. The translation from the uni-axial test data to true stress versus true effective plastic strain was performed using Equation (4.3) [16].

$$\begin{aligned}\varepsilon^{\text{true}} &= \ln(1 + \varepsilon^{\text{eng}}) \\ \sigma^{\text{true}} &= \sigma^{\text{eng}}(1 + \varepsilon^{\text{eng}}) \\ \varepsilon_{\text{eff, plastic}}^{\text{true}} &= \varepsilon^{\text{true}} - \frac{\sigma^{\text{true}}}{E}\end{aligned}\tag{4.3}$$

A mass density of  $2 \times 10^{-6}$  kg/mm<sup>3</sup> and a Poisson's ratio of 0.3, taken from literature, were used due to lack of data for these properties [21]. No strain-rate effects were implemented.

## 4.12 Simulation Setup

The experimental setup used by Agnew et al. (2015) was adapted when constructing the simulation setup [1]. The simulation setup incorporate two identical sets of support components consisting of: (a) bracket, (b) potting cup, and (c) potting, these are seen in Figure 4.5. The materials for each component is listed in Table 4.2. The measurements of the pots are extracted from laser scans of the complete ribs with pots attached, while the geometry of the p. cup is taken from CAD drawings of the experimental setup.



**Figure 4.5:** Support components including bracket (yellow), potting cup (blue), and pot (red). point **C** is center of pot and **a**=8.5 mm is the x-distance from **C** to rotational axis.

**Table 4.2:** Material parameters for support components in simulation setup.

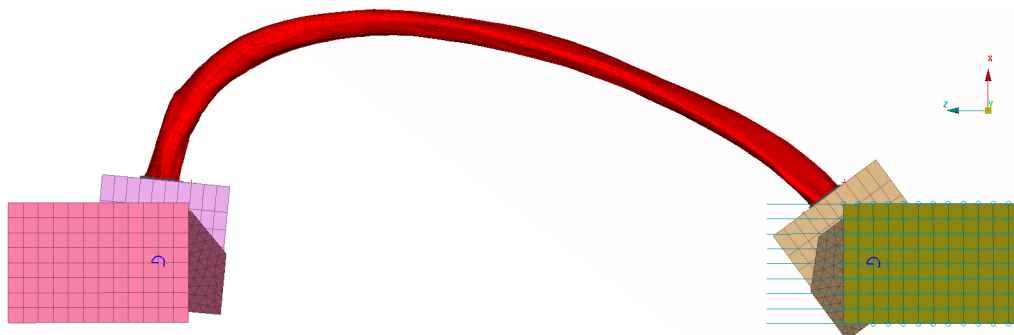
Support component	Young's modulus [GPa]	Mass density [kg/mm <sup>3</sup> ]	Poisson's ratio [-]	LS-DYNA material model
Bracket	-	$7.85 \times 10^{-6}$	-	*MAT_RIGID/*MAT_020
Potting cup	-	$2.7 \times 10^{-6}$	-	*MAT_RIGID/*MAT_020
Potting	2.2	$2 \times 10^{-6}$	0.34	*MAT_PIECEWISE_LINEAR_PLASTICITY /*MAT_024

The potting is constrained to the p. cup by adding all nodes on the bottom of the pot to the rigid p. cup using \*CONSTRAINED\_EXTRA\_NODES\_SET. The only permitted movement for the p. cup, relative to the bracket, is the single rotational degree of freedom about an axis normal to the loading plane, x-y plane in Figure 4.6. An important observation is that the axis of rotation is offset a distance of 8.5 mm

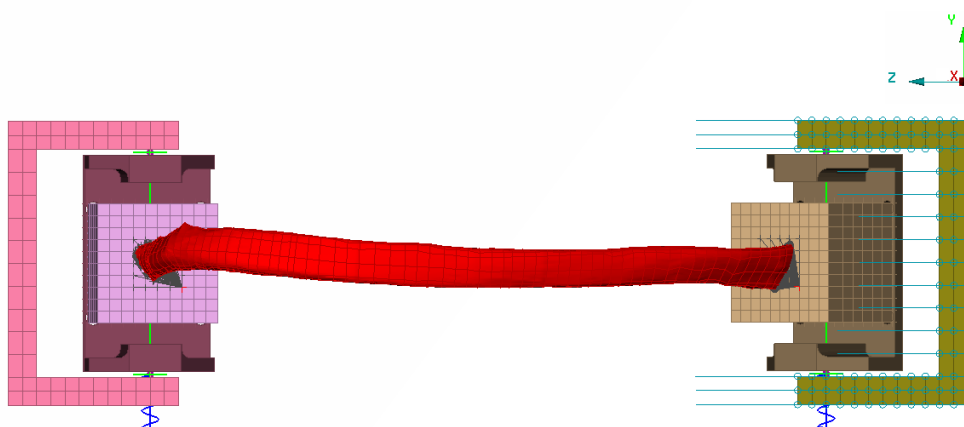
in relation to the center of the pot, seen in Figure 4.5. The offset is a consequence of the pot being mounted to the base of the p. cup.

The rotational degree of freedom for the p. cup is achieved by joining the bracket and p. cup together using a revolute joint defined by `*CONSTRAINED_JOINT_REVOLUTE`. The joint uses coincident nodal pairs belonging to the bracket and p. cup. A discrete element in the form of a torsion spring with a minimized finite stiffness is added between the p. cup joint node and bracket in order to measure the rotation in the joint.

In order to control the movement in z-direction (anterior-posterior) of the brackets a `BOUNDARY_PRESCRIBED_MOTION` was utilized on both brackets. For the anterior bracket the subject specific load curve, known from experiments, was used. A prescribed motion of zero was used on the posterior bracket to allow for measurement of the reaction force in z-direction through `BndOut`. Furthermore, both brackets were assigned a rigid material type which only permits global translations in z-direction.



(a) Side view.



(b) Top view.

**Figure 4.6:** The simulation setup with posterior left and anterior right.

### 4.13 Positioning of Meshed Rib Specimens

The positioning of a rib into the simulation setup was performed with the aid of subject specific triangulated surface meshes, computed from laser-scans, of the rib specimens including the pots. The laser-scan surfaces required alignment with the hexahedral mesh because of deviations in spatial orientation. The alignments were performed using transformation matrices generated with the open source 3D point cloud and mesh processing software CloudCompareV2 [30]. CloudCompareV2 utilizes the iterative closest point algorithm to minimize the distance between two similar meshes.

With the laser-scanned mesh aligned with the hexahedral mesh, seen in Figure 4.7, the positioning of the meshes were performed by following step 1-4 below.

1. Match the bottom and sides of the posterior pot from the setup with the posterior pot from the laser scanned surface.
2. Translate the anterior support components in z-direction to account for the rib specimens length.
3. Rotate the meshes together with the posterior pot and p. cup to allow for a visually acceptable fit between the anterior laser-scanned pot and setup pot.
4. Morph the height of the setup pots in order to align their top surfaces with the laser-scanned pots since the height of the pots differ slightly between specimens considering that the embedment process is done manually.

With the meshes properly positioned in the pots, at least three rows of circumferential nodes on the rib extremities were constrained to the closest nodes, on the pot surface, surrounding the rib using `CONSTRAINED_NODAL_RIGID_BODY`.



**Figure 4.7:** Hexahedral mesh (red) aligned with laser-scanned mesh (cyan).

## 4.14 Sensitivity Analysis of Rotation Axis

At an early stage in the project an analysis investigating the sensitivity to the position of the axis of rotation for the p. cup was deemed necessary. This, because of the different approaches concerning the p. cup seen when comparing the test procedures engineered by Charpail et al. (2005) and Kindig (2009), elaborated on in Section 2.3.

Three scenarios was tested to provide an indication on if and how the presence of a p. cup affected the behaviour of the rib when dynamically loaded.

Scenario (a) defines the baseline and utilizes the simulation setup, described in Section 4.12, without modifications. Scenario (b) is identical to scenario (a) except that the p. cup is massless. In scenario (c), the simulation setup, described in Section 4.12, does not employ a p. cup. Thus, the axis of rotation was positioned through the center of the pot and hence, effectively offsetting the axis of rotation a distance of 8.5 mm in the x-direction, seen in Figure 4.5.

Rib specimen K was chosen to carry out the sensitivity analysis on since it was the first rib to have a completed mesh.

## 4.15 Average Cortical Thickness

To assist the correlation comparison of the simulations, the average cortical thickness was extracted. Thin shells were produced for all ribs, described accordingly in Section 4.8, resulting in individual nodal thicknesses for all shell elements representing the cortical bone. The average cortical thickness  $t_{\text{avg}}$  was produced by weighting each averaged element thickness  $t_i$  with a weighting function  $w_i$  and summarize over all elements according to Equation 4.4.

$$w_i = \frac{dA_i}{A_{\text{tot}}} \quad (4.4)$$

$$t_{\text{avg}} = \frac{1}{N} \sum_{i=1}^N w_i t_i$$

$A_{\text{tot}}$  equals the total area of the shell,  $dA_i$  describes the element area and  $N$  quantifies the number of elements constructing the thin shell.

### 4.16 Natural Frequency Analysis

As a reaction to the obtained result from the simulations, a natural frequency analysis was conducted. The purpose of the analysis was to investigate the influence of the excitation signal that controls the motion of the anterior bracket and see if there is an excitation of the setups natural frequency. The frequencies under investigation were (a) the acceleration of the input signal and (b) the force output signal from a oscillation test. The input signal (a) is defined as the acceleration proportional to the force, as  $F = ma$ . The acceleration signal was extracted from  $t = 0$  until the criterion  $a(t_0) = 0$  was satisfied, i.e when maximum velocity was reached. At this point, little to no plastic deformation had occurred in the simulation. In the drop test, to obtain the output signal (b), the simulation runs normally until the extracted time  $t_0$ . The signal was then tapered off to zero and after that, the system was let free to oscillate with its natural frequency. The signals were then analysed using the Fast Fourier Transform (FFT) algorithm and extracted from the single-sided amplitude spectrum.

# 5

## Results

In this chapter the results from the different modeling approaches are presented. Also an assessment of the mesh quality and energy can be seen. Lastly, the influence from the natural frequency analysis is presented.

### 5.1 Energy Balance and Mass Scaling

Based on the theory and suggested conditions presented Section 3.9, the models were evaluated in regards to the energy balance.

For all models, the recorded maximum deviation in the energy ratio was 0.1 %, while the maximum contribution from the HG control to the total energy was 0.12 %. Both these values are well below the 5 % and 10 % condition for energy ratio and HG control, respectively.

The maximum mass increase due to the mass scaling was 3.14 % while the mean was calculated as 2.31 %. The effect of mass-scaling up to 2.88 % was tested on Rib K and compared with an identical simulation without mass-scaling. No difference in the results were observed.

For model specific information, the interested reader is referred to Table A.1 in Section A.1.

### 5.2 Hex-Thick Shell Modeling Approach

Stability problems were experienced during the simulation of the thick shell cortical representation. For seven of the ribs where the HS approach was applied, the HTS was also evaluated. All but two managed to finalize the simulation without error termination. Rib K and J error terminated due to the appearance of negative volume. This was at the time where plastic deformation tended to initialize,

comparing to the other simulations. The ribs that finalized the simulation however, did not attain acceptable results due to an energy balance not meeting the criteria specified in Section 3.9. Energy was introduced artificially possibly from numerical instabilities.

Measures to obtain agreeable results were taken, such as reduced time step TSSFAC factor, additional accuracy control and tuned hourglass control coefficient. Though, some of the measures helped to achieve normal termination the energy balance was still not acceptable. The energy balance is presented in Table A.1 in Appendix A.1.

### 5.3 Mesh Quality

The mesh quality of the investigated rib specimens were evaluated based on the three different metrics: aspect ratio (AR), angle idealization and Jacobian, as described in Section 3.8. The mesh quality assessments are listed in Table 5.1.

**Table 5.1:** Mesh quality metrics for all rib specimens.

# Rib	# Elements	AR >3 [%]	AR >10 [%]	AR $\equiv$ 5% [%]	Angle 90 $\pm$ 45 [%]	Angle 90 $\pm$ 70 [%]	Jacobian $\leq$ 0.7 [%]	O-grid
Rib A	$1.53 \times 10^6$	4.44	0.01	2.9	6.44	0.48	0	No
Rib B	$1.35 \times 10^6$	2.34	0.00	2.7	8.27	0.82	0	No
Rib C	$1.13 \times 10^6$	5.33	0.01	3.1	4.25	0.38	0	No
Rib D	$9.45 \times 10^5$	5.07	0.01	3.0	8.39	0.71	0.001	No
Rib E	$6.46 \times 10^5$	4.3	0.00	3.0	5.19	1.16	0	No
Rib F	$8.59 \times 10^5$	4.62	0.01	2.9	3.61	0.53	0	No
Rib G	$7.40 \times 10^5$	7.4	0.01	3.3	3.74	0.50	0	No
Rib H	$7.19 \times 10^5$	3.27	0.02	2.8	4.73	0.73	0	No
Rib I	$8.25 \times 10^5$	2.53	0.00	2.7	4.02	0.67	0	No
Rib J	$1.38 \times 10^6$	5.08	0.03	3.0	7.04	0.51	0	No
Rib K	$6.14 \times 10^5$	25.30	0.05	4.4	9.23	0.99	0	Yes x4
Rib L	$1.13 \times 10^6$	22.1	0.58	5.4	6.90	0.12	0	Yes x2

From Table 5.1 and 5.2 it can be concluded that all meshes except those for rib specimens K and L, satisfy or are in close agreement with the conditions set on the three mesh metrics.

1. Less than 5% of the elements exhibit an AR>3.
2. Less than 5% of the internal angle measurements exhibit an absolute deviation exceeding 70°.
3. (a) Jacobians should have a positive value, (b) The Jacobian should preferably be greater than 0.2, (c) less than 5% of elements should have a Jacobian greater than or equal to 0.7.

The two rib specimens, Rib K and Rib L, which do not satisfy the mesh requirements on AR, were both meshed using O-grids. Because of time constraints, these two rib specimens were not re-meshed with the meshing methodology used for the remaining ten rib specimens. It should however be noted that 95% of the elements have an AR



equal or below 4.6 and 5.2, for rib specimen Rib K and Rib L respectively. Thus, the AR violation of the offending elements are relatively low.

**Table 5.2:** Mesh quality shell.

# Rib	Type	# Elements	AR >3 [%]	Angle 90±45 [%]	Jacobian ≤ 0.7 [%]
Rib C	Shell	$1.37 \times 10^5$	1.48	0.00	0.00
	Solid	$8.41 \times 10^5$	3.75	5.25	0.00
Rib E	Shell	$7.50 \times 10^4$	0.59	0.08	0.00
	Solid	$5.00 \times 10^5$	1.28	6.12	0.00
Rib F	Shell	$1.17 \times 10^5$	0.10	0.00	0.00
	Solid	$6.33 \times 10^5$	3.20	4.86	0.00
Rib H	Shell	$9.51 \times 10^4$	0.00	0.00	0.00
	Solid	$5.32 \times 10^5$	0.42	6.40	0.00
Rib I	Shell	$9.99 \times 10^4$	0.00	0.00	0.00
	Solid	$6.24 \times 10^5$	1.74	5.28	0.00
Rib J	Shell	$1.27 \times 10^5$	0.05	0.00	0.00
	Solid	$1.10 \times 10^6$	2.89	9.53	0.05
Rib K	Shell	$8.17 \times 10^4$	4.91	0.00	0.00
	Solid	$4.50 \times 10^5$	29.66	11.90	0.08

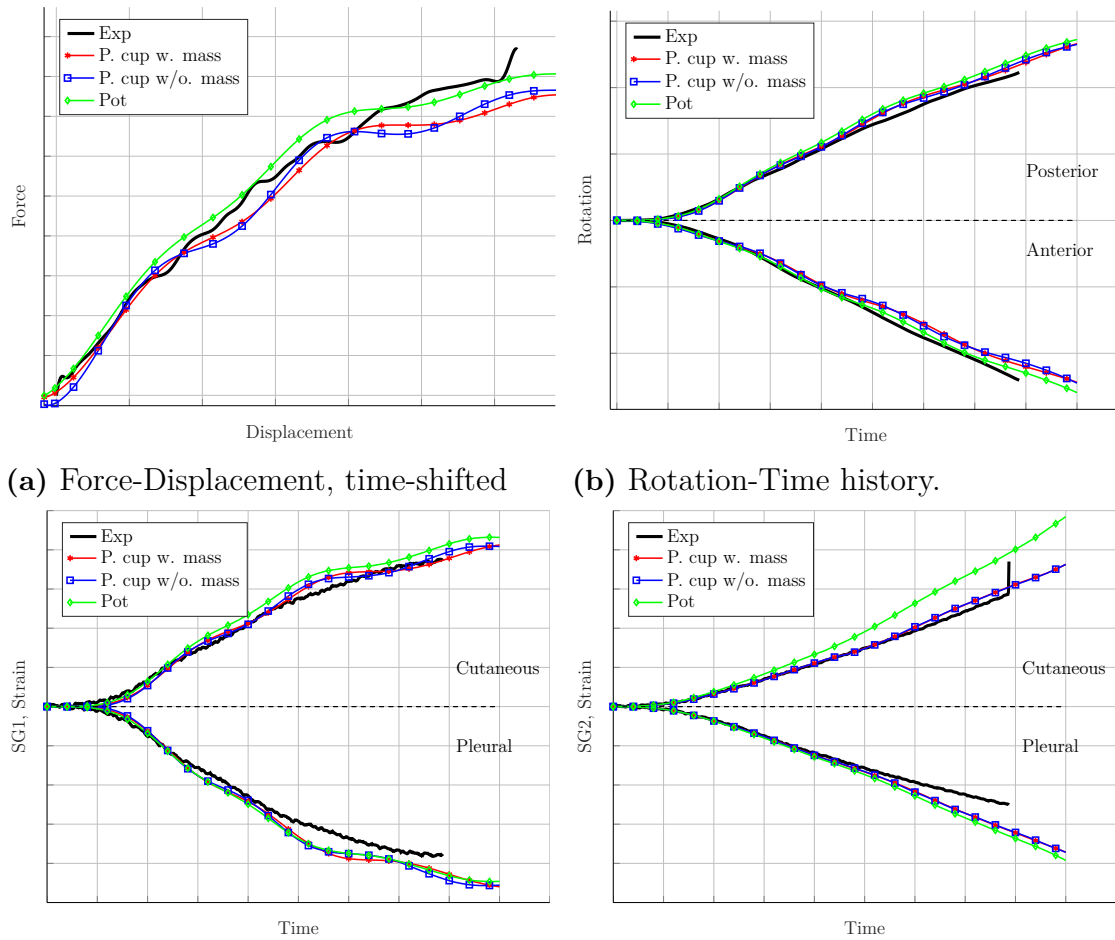
## 5.4 Sensitivity Analysis of Rotation Axis

The aim of the sensitivity analysis, as described in Section 4.14, was to study the effect on the results from the presence of a p. cup. In Figure 5.1, a relative comparison is seen between including a p. cup, with and without mass, and only considering the pot. To allow for a fair comparison, all simulations used the most detailed AHM approach for modeling the rib.

From Figure 5.1, it can be concluded that the mass of the p. cup has no significant effect on the rib's stiffness behaviour, rotation nor strain. Although, a difference in the stiffness behaviour is observed when the p. cup is excluded and instead, the axis of rotation is positioned through the mass centre of the pot. Also, a slightly greater rotation for the anterior rib extremity is seen when the p. cup is excluded. Thus, it is shown that the position of the axis of rotation has an effect on the stiffness response of the rib as well as a slight effect on the anterior rotation.

The strains observed in the three simulations are in close agreement, with the exception for the cutaneous strain gauge measured at 60% of the curve length. The higher tensile strain recorded at the strain gauge closest to the experimental fracture location, implies that the first principal Green strains are locally higher in the fracture site for the pot simulation compared to the other two simulations. This observation was further supported when studying the first principal Green Strain of the cortical bone for the whole rib. At the experimental fracture time, the model

## 5. Results



(c) Strain gauge-Time history at 30% of curve length. (d) Strain gauge-Time history at 60% of curve length.

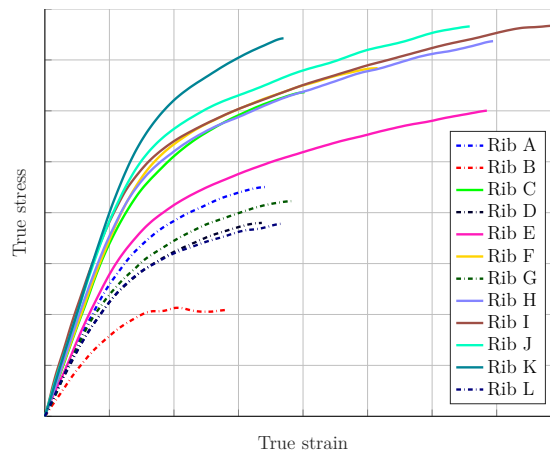
**Figure 5.1:** Simulation comparison with experiments for rib specimen K. Fracture occurs at 39.35 ms.

predicted peak strain was 45 % higher for the pot compared with the p. cup. Further away from the fracture site the strain deviations between the simulations decline.

### 5.5 Force-Displacement Response

The load carrying capabilities of the rib is dependent on the cortical bone and its properties. Therefore it is of interest to examine the true stress-strain curves from the subject specific cortical coupon tests. In Figure 5.2, the result is seen. Seven out of twelve ribs, Rib C,E-F,H-K, have a higher Young's modulus and a more prolonged plastic region compared with the remaining five ribs.

When studying the force-displacement match for the numerical data, the same division for the ribs can be made. For the same seven out of twelve ribs, the force-



**Figure 5.2:** True stress-strain response for subject specific cortical coupon tests conducted in [2].

displacement response is in good agreement with the experimental data, independent of the modeling approach. For the remaining five ribs, independent of the modeling approach, the match was not considered satisfactory. The AHM approach CORA score for the two groups is seen in Figure 5.4a. In Figure 5.3, Rib C with a AHM CORA score of 0.839, and Rib G, with a AHM CORA score of 0.663 can be seen to help exemplify a curve-to-curve comparison in good agreement and one that is not.

A paired two-tailed t-test was conducted on the full sample of twelve ribs to determine whether there was a statistically significant difference in the CORA force-displacement rating for the AHM compared to the AHV approach. Consequently,  $\mathcal{H}_0 : \mu_d = 0$  and  $\mathcal{H}_1 : \mu_d \neq 0$ .

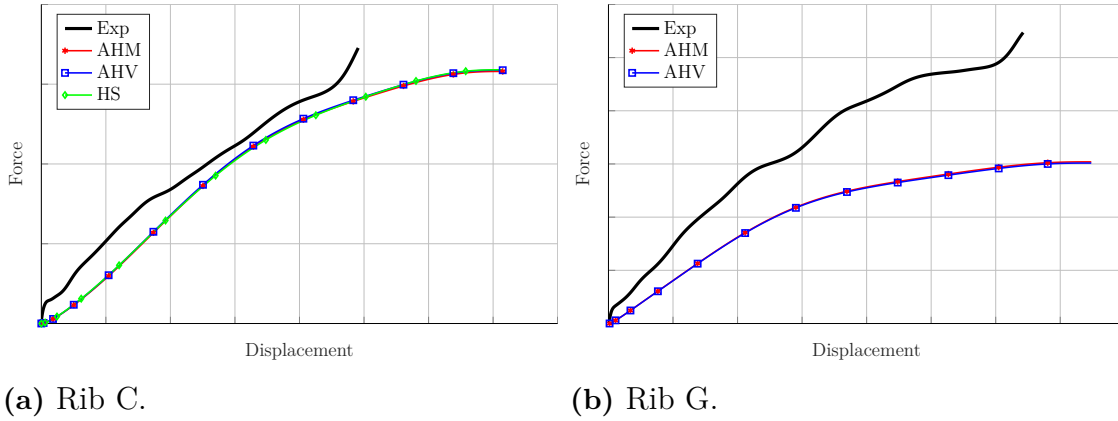
The AHM approach resulted in a CORA force-displacement rating of  $0.778 \pm 0.127$  (mean  $\pm$  std) as opposed to the AHV approach  $0.771 \pm 0.126$  (mean  $\pm$  std). It was concluded that the t-test does not reject the null hypothesis at the 5% significance level ( $p = 0.0543 > 0.05$ ). Thus, there is no statistically significant difference in the CORA force-displacement ratings between the AHM and AHV approach.

Another paired two-tailed t-test was conducted on a sub-sample containing the seven ribs C,E-F,H-K which was also modeled using the HS approach. This, to determine whether there was a statistically significant difference in the CORA force-displacement rating between the AHM and HS modeling approach. Consequently  $\mathcal{H}_0 : \mu_d = 0$  and  $\mathcal{H}_1 : \mu_d \neq 0$ .

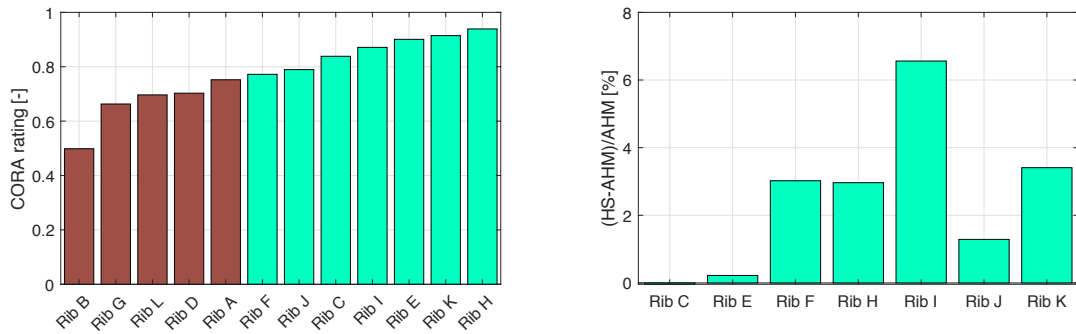
The AHM approach resulted in a CORA force-displacement rating of  $0.861 \pm 0.0634$  (mean  $\pm$  std) as opposed to the HS approach  $0.882 \pm 0.0707$  (mean  $\pm$  std). It was concluded that the paired t-test rejects the null hypothesis at the 5% significance level ( $p = 0.0287 < 0.05$ ), so there is a statistically significant difference in CORA rating.

## 5. Results

By studying the CORA force-displacement rating in detail for the seven shell meshed ribs it is seen in Figure 5.4b that all except one rib, Rib C, have a better matching force-displacement behavior compared with the AHM approach. The interested reader is referred to Section A.2 to make the same conclusion.



**Figure 5.3:** Non time-shifted force-displacement responses.



**(a)** AHM approach.

**(b)** Difference between AHM and HS approaches.

**Figure 5.4:** Force-displacement CORA ratings.

## 5.6 Rotations

The anterior and posterior rotations in the simulations was compared with the experimental data using CORA. No visual deviations between the posterior nor the anterior numerical rotations was seen when comparing the AHM, AHV and HS modeling approaches. This is further emphasized when comparing the posterior and anterior mean and standard deviation presented in Table 5.3.

In Figure 5.5b, the rotations of Rib D for all modeling approaches as well as for the experiment, is seen. Rib D has a CORA rating of 0.881 and 0.980 for the anterior and posterior end, respectively.

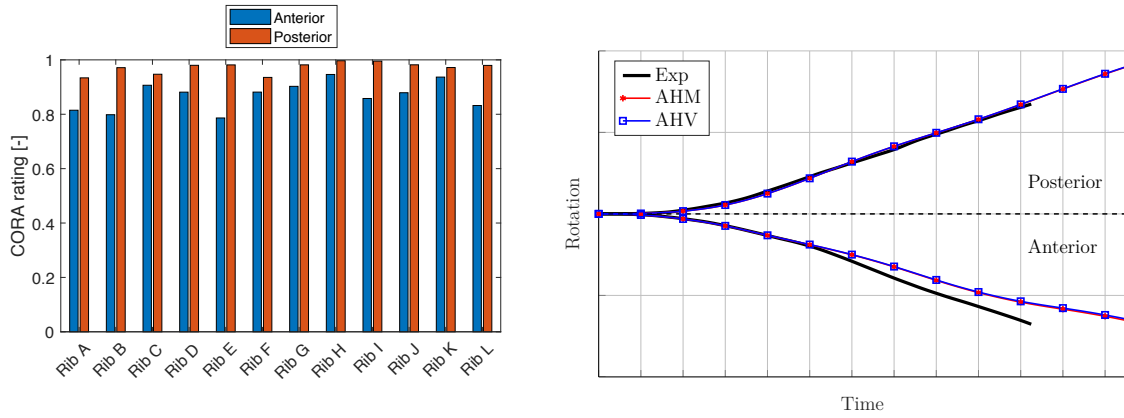
**Table 5.3:** Mean and standard deviation of CORA rotations rating.

Sample size	Side	Approach	Mean	Std
All ribs	Ant	AHM	0.869	0.0520
		AHV	0.865	0.0529
	Post	AHM	0.971	0.0213
		AHV	0.971	0.0215
Rib C,E-F,H-K	Ant	AHM	0.885	0.0539
		AHV	0.881	0.0558
		HS	0.888	0.0556
	Post	AHM	0.973	0.0235
		AHV	0.973	0.0242
		HS	0.973	0.0206

In Figure 5.5a, it is seen that the posterior rotations are in closer agreement with the experiment compared with the anterior rotations for the AHM modeling approach. This is the case for all rib specimens as well as for all modeling approaches.

The absolute value of the anterior rotations predicted in the simulations are, independent of modeling approach, smaller than the corresponding experimental absolute values, measured at the fracture time. The mean $\pm$ std percentage difference, measured at fracture time, with respect to the experimental values for the ribs modeled with the AHM, AHV and HS approach are  $19.1\pm 9.44$ ,  $20.0\pm 9.65$ , and  $20.1\pm 11.9$ , respectively.

An analysis was conducted to investigate if the observed anterior rotations in the FE models could be explained by a too weak potting material, allowing relative movement between the submerged rib end and p. cup. The Young's modulus of the potting material was reduced with a factor of ten. The weakened material had no visual affect on the rotations and no relative movement was observed.



(a) CORA rotation rating for AHM.

(b) Rotation comparison for Rib D.

**Figure 5.5:** Rotation comparison.

## 5.7 Strain-gauges

The strain gauge data measured in the experiment was compared with the numerical strain gauge data. Overall, the uni-axial strain is considered to correspond well with the experimental data for all strain gauges as well as for all modeling approaches. In Table 5.4, the mean and standard deviation for respectively strain gauge is seen.

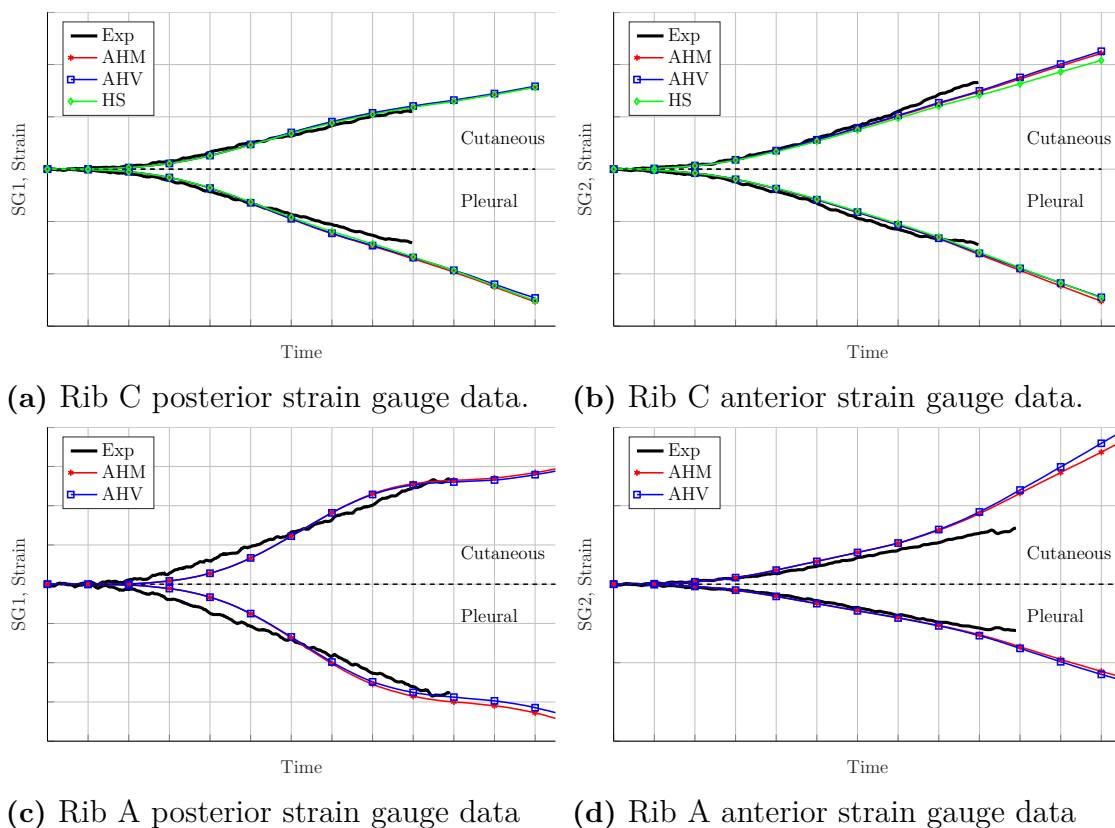
To exemplify the CORA rating for a good and a poor agreement with experimental data, the curve-to-curve comparisons for all four strain gauges pertaining to Rib C and Rib A, respectively, are seen in Figure 5.6. The AHM CORA rating  $\text{mean} \pm \text{std}$  for all four strain gauges were  $0.944 \pm 0.034$  and  $0.871 \pm 0.049$ , for Rib C and Rib A, respectively. To be compared with  $0.885 \pm 0.102$ , for all twelve ribs and strain gauges using the AHM approach.

A paired two-tailed t-test was conducted on the full sample of twelve ribs, including all four strain gauges for each rib, to determine whether there was a statistically significant difference between the CORA strain gauge rating when the simulation was run using the AHM compared to the AHV approach. Consequently,  $\mathcal{H}_0 : \mu_d = 0$  and  $\mathcal{H}_1 : \mu_d \neq 0$ .

The AHM approach resulted in a CORA strain gauge rating of  $0.885 \pm 0.102$  (mean  $\pm$  std) as opposed to the AHV approach  $0.885 \pm 0.102$  (mean  $\pm$  std). It was concluded that the t-test does not reject the null hypothesis at the 5% significance level ( $p = 0.965 > 0.05$ ). Thus, there is no statistically significant difference in the CORA overall strain gauge ratings between the AHM and AHV approach.

**Table 5.4:** Mean and standard deviation of the CORA ratings for the strain gauge data.

Sample	Gauge	Approach	Mean	Std
All ribs	CSG1	AHM	0.907	0.057
		AHV	0.889	0.064
	CSG2	AHM	0.915	0.093
		AHV	0.927	0.062
	PSG1	AHM	0.812	0.119
		AHV	0.814	0.130
	PSG2	AHM	0.909	0.101
		AHV	0.910	0.106
Rib C,E-F,H-K	CSG1	AHM	0.889	0.052
		AHV	0.877	0.056
		HS	0.919	0.048
	CSG2	AHM	0.918	0.107
		AHV	0.938	0.056
		HS	0.944	0.049
	PSG1	AHM	0.862	0.064
		AHV	0.870	0.073
		HS	0.883	0.067
	PSG2	AHM	0.892	0.127
		AHV	0.886	0.132
		HS	0.900	0.108

**Figure 5.6:** Strain gauge-Time history for (a-b) good agreement, (c-d) poor agreement.

A paired two-tailed was conducted on Rib C,E-F,H-K, including all four strain gauges for each rib, to determine if a statistically significant difference could be established between the CORA strain gauge rating comparing the AHM and HS modeling approaches. Consequently,  $\mathcal{H}_0 : \mu_d = 0$  and  $\mathcal{H}_1 : \mu_d \neq 0$ .

The AHM approach resulted in a CORA strain gauge rating of  $0.890 \pm 0.0897$  (mean  $\pm$  std) as opposed to the HS approach  $0.911 \pm 0.0719$  (mean  $\pm$  std). The paired two-tailed t-test rejected the null hypothesis at the 5% significance level ( $p = 0.00824 < 0.05$ ). This, implies that the HS approach results in strain gauge predictions which differs from the AHM approach predictions.

The results from the two t-tests are supported by a visual inspection of the strain gauge plots for all ribs. These are seen in Section A.2. However, the statistically significant difference seen in the t-test when using the HS modeling approach is not obvious based on a visual inspection.

## 5.8 Fracture Location


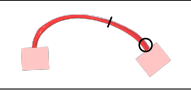
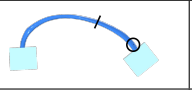


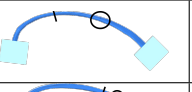

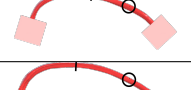
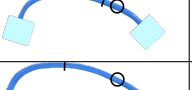
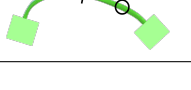

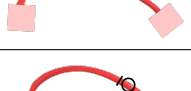
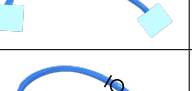

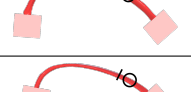
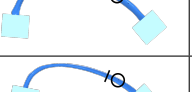
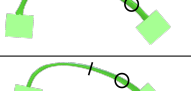

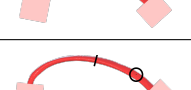
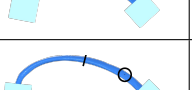


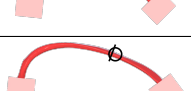


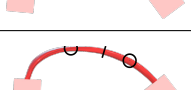
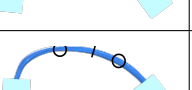
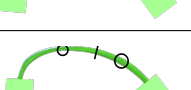
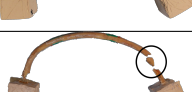
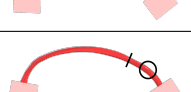
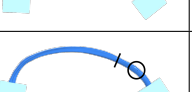
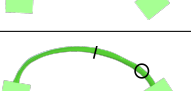
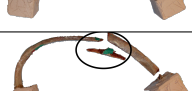
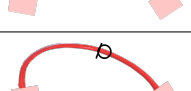
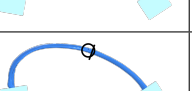
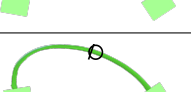

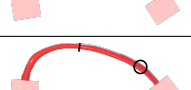
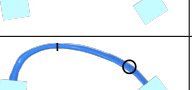
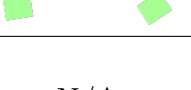
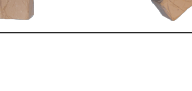
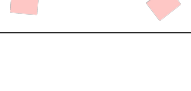

In Table 5.5, the assessment of all simulated ribs and modelling approaches are visualized. The rib fracture location metric, defined in Section 4.3, declares if the correct fracture location has occurred followed by a visual inspection. In a second step, the correlation to the force-displacement curves, as well as the remaining output data, is established and a complete judgment can be made. For the all-Hex approaches, fracture was predicted for Ribs C, E, F, H, J and K. These ribs all possess material data from the upper spectra of the material stress-strain response and attain a force-displacement curve with higher CORA values. The opposite is seen for the Ribs A, B, D, G and L where the fracture location was observed at a location not coinciding with the experiment.

Examining the AHM approach for Rib C, it can be seen that the fracture location appears to be too posteriorly located. However, as the mapping source mesh was inadequate, the global stiffness was considered to be more accurately captured in the AHV approach and is therefore treated as a success. The first refinement step by the AHV approach was deemed successful for all ribs in the sense that the results did not change, except the previously treated Rib C. Nevertheless, the HS simulations



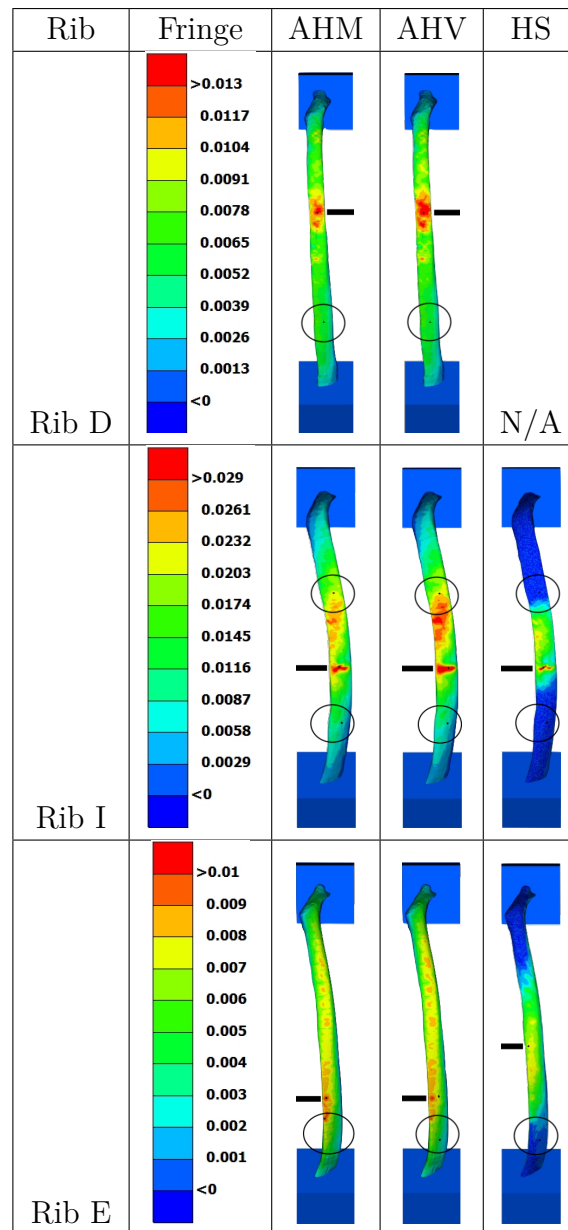
only resulted in two correct predictions of the fracture location.

**Table 5.5:** Fracture location for post-test experiment (circle) and all undeformed modeling approaches (line).

Rib	Exp	AHM	AHV	HS
Rib A				N/A
Rib B				N/A
Rib C				
Rib D				N/A
Rib E				
Rib F				
Rib G				N/A
Rib H				
Rib I				
Rib J				
Rib K				
Rib L				N/A

Inspecting the first principal strain visualized on the rib geometry at the time of fracture in Table 5.6, it is seen that the HS approach results in a different strain concentration distribution. As the shell elements stray from the 3D stress-state, this discloses on the theory that a 2D stress-state cannot fully comprehend the out-of-plane shear occurring in the simulations and effectively, the strain concentration field narrows.

**Table 5.6:** Cutaneous view of modeling approaches at experimental fracture time with first principal strain showing. Experimental (circle) and simulation (line) fracture location.


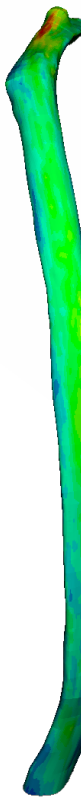


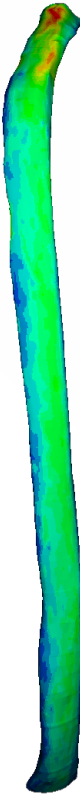

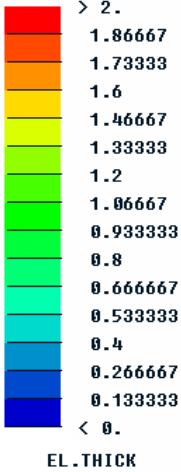


For Rib I, a distinct strain concentration can be seen between the two fractures occurring in the physical test. When comparing this figure to the illustration of the thickness in Table 5.8, a distinct thickness deficiency is seen at the same location. After further investigation, this rib was concluded to be treated as an outlier due to a deficiency most likely emerging in the CBM method.

## 5.9 Cortical Thickness

The cortical thickness distribution of the ribs is found in Table 5.7 and 5.8. Rib I is treated as an outlier and is excluded from the thickness analysis.

**Table 5.7:** Cortical thickness distribution of ribs where fracture location was predicted.

Rib	C	E	F	H	J	K
						
						
Avg. thickness [mm]	0.577	0.695	0.598	0.636	0.715	0.834

By ocular assessment of Table 5.7, the thickness appears uniformly distributed over the longitudinal center line of all ribs, except for Rib F. This differs from the ribs where fracture location occurred inconclusive, as the ribs in Table 5.8 appears with prominent thickness deficiencies. The average cortical thickness is also found to be lower for this set of ribs. With an average thickness of 0.596 mm, they are on average 0.08 mm thinner compared to 0.676 mm for the set of ribs where fracture location was predicted. Additionally, the average age is also 12.2 years higher,  $80.4 \pm 10.6$  (mean $\pm$ std) compared to  $68.2 \pm 12.2$  (mean $\pm$ std). This coincides with the findings presented in Section 2.2.2, that loss of stiffness due to, inter alia, decreasing bone thickness correlates to increasing age.

**Table 5.8:** Cortical thickness distribution of ribs where fracture location was inconclusive.

# Rib	A	B	D	G	I	L
<p>EL.THICK</p>						
Avg. thickness [mm]	0.523	0.604	0.618	0.623	0.789	0.612

## 5.10 Natural Frequency Analysis

Due to Rib Bs modest performance in coinciding with the experimental data along with weak material data pertaining to its cortical stress-strain curve, it was chosen to represent the set of ribs where fracture was unable to predict in the natural frequency analysis. Rib H has both high Young's modulus with a prominent plastic region in the stress-strain curve and well corresponding results to the experimental data. Therefore, it was selected to represent the spectra of ribs with high stiffness accurately predicted fracture location predicted.

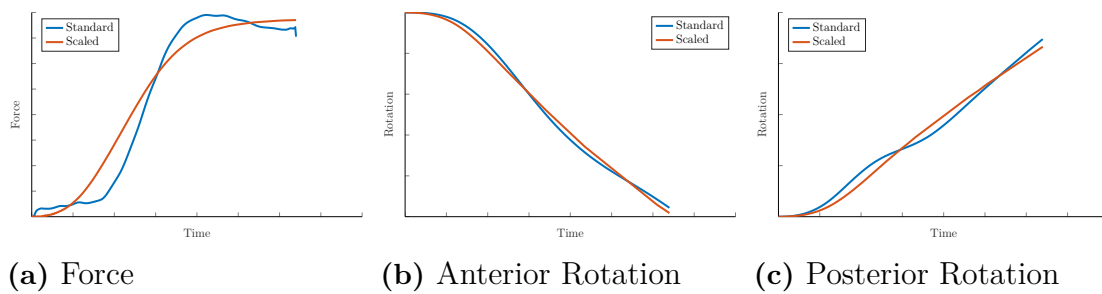
For Rib B, two natural frequencies were clearly identified from the oscillation simulation. A lower frequency of 4.65 Hz, which corresponds to the anterior-posterior oscillation and one slightly higher frequency of 60.49 Hz from the rotation of the p. cup. The frequency extracted from the input signal has a peak value at 71.43 Hz, which is fairly close the natural frequency of the simulation setup.

The same tendencies were seen in the oscillation simulation of Rib H, though with the generally higher frequencies of 7.41 Hz and 125.9 Hz. However, this was expected

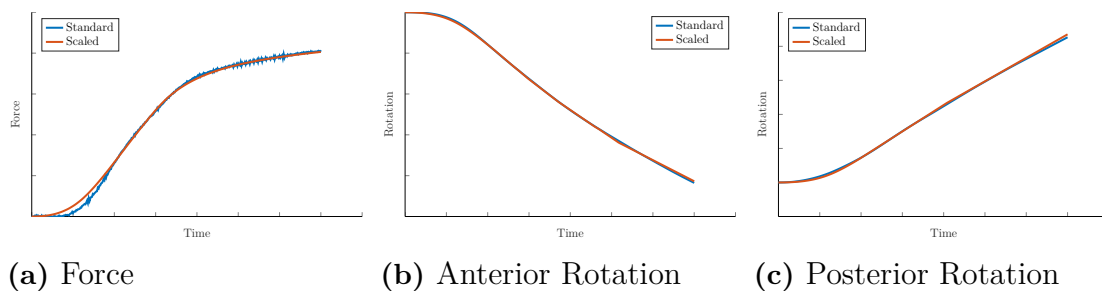
since frequency is defined as  $\omega_n = \sqrt{k/m}$  and Rib H possesses a higher Youngs modulus. The input signal yields the frequency of 76.92 Hz and therefore is the natural frequency of the stiff ribs less prone to be excited by the input signal.

To complement this analysis, a scenario where the input velocity and time duration was scaled to perform the same displacement, was conducted. Thus, the excitation frequency is moved towards the lower side of the frequency domain. This affects the frequency of the excitation as well as the dynamic equilibrium in the simulation. Observing the force, the anterior rotation and the posterior rotation curves in Figure 5.7 respectively, an oscillating behavior in the standard simulation can be identified. These results corresponds to the findings regarding the excitation of the natural frequency in the simulation of Rib B. However, the fracture location was left unaffected.

Affirming the results regarding the natural frequency of Rib H can be seen in Figure 5.8. Here, there is no oscillating behaviour seen in the standard simulation, which confirms the theory that a stiffer response yields a reduced chance of amplifying the natural frequency.



**Figure 5.7:** Rib B: Comparison of the standard case and the scaled velocity simulation.



**Figure 5.8:** Rib H: Comparison of the standard case and the scaled velocity simulation.



# 6

## Discussion

This thesis aims to develop a methodology to model ribs using finite elements and, by explicit FE LS-DYNA simulations, determine rib fracture location based on a first principal strain concentration assumption. Twelve ribs were modelled, with all hexahedral elements attaining subject specific properties and three element through-the-thickness in the cortical bone, to be arranged in a setup where rib fracture was evoked. By comparison with data from physical testing, fracture was predicted on six ribs whereas six rib simulations resulted in inconclusive fracture location. Homogenised trabecular material properties was applied to all twelve ribs, where only one rib had a different response in the fracture location. Further simplification measures were applied to the six ribs which correctly predicted the fracture location by replacing the cortical hexahedral elements by a thin shell. While the CORA ratings, established in the thesis, were slightly higher for the hex-shell approach, the fracture location was merely predicted accurately on two of the six ribs. Consequently, the prevailing 2D stress-state in the shell element formulation condemns the ability to capture the out-of-plane strains.

The discussion aims to assess the modelling approaches and what is simplified and therefore missed in the shell formulation. The reason behind why Rib I was treated as an outlier will be given as well as reflections about the discrepancy in response for the two groups of ribs regarding fracture location. The data provided to the thesis and the output data from the simulations will be evaluated and comments on the method of assessing the rib fracture will be presented. Lastly, the entire structure of investigating this issue during a Masters thesis will be addressed briefly.

The methodology used to assess the fracture location is dependent on the ability of the FE rib model to replicate the experimental response without optimization of material properties and thus establish confidence in that, given a validation in close agreement, the fracture time should also coincide with the experiment. This methodology, although only applicable to subject specific modeling, does not run the risk of tuning the model in such a manner that possible shortcomings are unintentionally built in. A consequence of not optimizing the data is that failure strain proves hard to define for the FE model. Only the uni-axial strain, measured at four locations, is known from the experimental tests. Hence, not the failure strain required to initiate the fracture. So, the fracture strain in the FE model needs to

be either, optimized based on literature before being applied, or based on the rupture point derived from the coupon test. Neither of these proposals are justified. The optimization does not add any information to the model, it merely tunes it to behave in an anticipated way. The tension test only provides the uni-axial rupture strain, not necessarily comparable to the first principal strain due to the missing out-of-plane contributions.

The fracture location metric, with the accompanying 15 % limit, was shown to provide a justifiable quantification on how well the fracture location was predicted compared with the experiment. The grounds for stating this is the visual comparison of the fracture location, made possible in Figure 5.5. The comparison is considered to support the use of the fracture location metric. The deviations allowed within the 15 % limit are considered reasonable since the distribution of the first principal strain concentration often covers a region in which the peak strain element is located, as indicated in Table 5.6. In reality, all structures have imperfections, such as for example micro cracks, which might to some degree govern the exact fracture location. The FE model do not contain that level of detail which warrants an interval as a feasible measure in which the fracture should be found. Additionally, the unquantifiable measurement errors support the use of an interval instead of a single value.

The posterior pot rotations were seen to agree well with the experimental data. However, the anterior end rotated less in absolute terms, compared with the experiment, independent of modeling approach. Also, the deviations were observed to increase from the birth of plastic strain in the model up to the time of fracture. A reason explaining this behaviour, which allowed to be tested, could not be found. Although, hypothesis were investigated without providing a definite explanation. For instance, the stiffness of the pot material was lowered with a factor of ten to test for relative movement between the pot and rib end. It was shown to have no effect on the results. The sensitivity analysis provided evidence that the rotations are affected by the position of the axis of rotation. But since the potting cup was taken from the CAD geometry, used to build the test rig, the axis of rotation should be accurately represented. The last hypothesis, which was not tested, is that the lack of element erosion might have an affect on the anterior rotation since the fractures are commonly observed to occur anteriorly on the rib. Rib I was excluded from the analysis after analysing the thickness distribution and the first principal strain at the fracture time. From Table 5.6 and 5.8 it was concluded that the strain concentration was a consequence of the thickness deficiency found exactly at the same location. Rib I possess material properties, age and average cortical thickness seen in the set of ribs where fracture location was predicted. Tendencies of higher strain in the region close to where fracture occurs in the physical test can also be seen. By further investigating the periosteal and endosteal surfaces handed to the project, the thickness deficiency was believed to have emerged in the CBM procedure of the CT-data. It was consequently considered an outlier and was not treated further.



Regarding the modelling approach, the HS approach manages to perform slightly better when assessing the correspondence to experimental data in all measured parameters except fracture location. This is believed to be governed by the difference in element theory, which here results in a stiffer response which comply better with the experimental data, disregarding the fracture location. It could also be due to the added material that fills the void created between the shell and the trabecular property in this modelling procedure. However, the largest differences were seen when analyzing the fracture location. First principal strain is a measure that accounts for the in-plane as well as the out-of-plane strain. When applying shell theory, the ability to capture out-of-plane strains diminishes and regions where the out-of-plane strain contribution is significant, will simply vanish in comparison to regions with higher tensional strain. However, the 3D stress state seen in the hexahedral representation of the cortical bone allows for the out-of-plane strains to be captured which was shown to be key in predicting the fracture location accurately.

The CORA value of the force-displacement curves was proven to correlate to whether the fracture location could be accurately predicted or not. A line could be drawn to separate the two sets of ribs accurately predicting the fracture and those that do not. Furthermore, the predicted fracture location is strongly correlated to the material data, as higher Young's modulus and a more prolonged plastic region was seen in the ribs for which the fracture location was predicted. For ribs where the fracture location was inconclusive, both the plastic region and the Young's modulus was reduced. This raised a new hypothesis; the quality of the material data corresponds to the ability to predict fracture location. The average age, average cortical thickness and the thickness distribution are measures that are contributing to an accurate representation of the cortical bone. As described in Section 3.1, the microstructure of the human rib is a complex structural composition consisting of pores that proliferates when aging occur. Thus, the porosity is affecting the ability to detect and predict a distinct border between cortical and trabecular bone. The porosity effect is also believed to influence the coupon tests, as pure bone fragments without any discontinuances prove harder to extract and thus, the probability of substandard quality coupons increases. Subsequently, the possibility of micro cracking and crack initiation becomes more prominent as the regions with lower bone quality increase, generated by higher porosity.

The performance of the CBM method is also reduced as a consequence of an increased presence of porosity. It is impossible to define a distinct border using a 6-parameter step model if there is no distinct border to be found to begin with. A shortcoming of the CBM method is that the algorithm is designed to search for a start and an end coordinate of the cortical bone and therefore lacks the ability to capture voids encapsulated inside the cortical bone. Even if the CBM algorithm were to be altered to deal with the possibility of porosities, the underlying CT image resolution needs to be sufficiently high to enable the voids to be distinguished.

The reasoning stated in the two previous paragraphs, generates the foundation to why five of the ribs did not perform as intended. The PMHSs had an average

age of 80.4; 12.2 years higher than in the fracture location predicting set of ribs. As expected for this set, the average cortical thickness was 11.8% thinner and the thickness distribution portrayed itself in a discontinuous manner, seen in Table 5.8. The strain concentrations could also be correlated to regions of thinner cortical bone.

The reasoning can also be applied to the predictability observed in the set of ribs where fracture location was accurate. These ribs possess an average thickness of 0.676 mm with a continuous thickness distribution, highlighted in Table 5.7. Hence, the strain concentrations are not concentrated to local jumps in thickness, but rather governed by the rib's global bending response. The average cortical thickness is also comparable to the one found in the THUMS model [21]; 0.676 mm compared to THUMS 0.7 mm.

The issue under investigation was considered to be well suited as a Master's thesis project. It contains the ability to conduct valuable research within a relevant field of vehicle safety and human body modelling. The results from this thesis have the potential to provide valuable guidelines when further developments of thorax in human body models is to be undertaken.

# 7

## Conclusion

It has been demonstrated that the rib fracture is strain controlled in the investigated dynamic loading condition and that the rib fracture location, as well as the structural response, can be accurately predicted when modeling the cortical and trabecular bone using a single averaged material property for the cortical and trabecular bone, respectively. In addition, the cortical and trabecular bone must be modeled using an element formulation that supports a 3D stress state. This modeling approach represents the lowest level of complexity required to capture the full rib response during an anterior-posterior dynamic loading.

Even though the recommended modeling approach has the ability to predict a subject specific rib response, it still requires correct input data for the cortical bone in the form of geometry and material properties. The geometry provided by the CT imagery processing and the material properties of the rib, must accurately represent the tissue-level properties of the cortical bone. The CBM method, which provides the rib geometry, lack the ability with the available HRclinCT resolution, to capture the effects of cortical bone porosity. This will lead to a misrepresented cortical bone and a numerical rib model, which regardless of ability, will fail in predicting the anticipated rib response.



# 8

## Further Work

As the modelled ribs contains on average  $9.9 \times 10^5$  elements, the modeling approach cannot be directly industrialized and transferred into a HBM. It is therefore suggested to perform a step-wise increase of the element size on a generic rib and evaluating each reduction against a fine meshed model. To allow for a larger element size, the number of elements through-the-thickness of the cortical bone must be reduced to maintain an acceptable aspect ratio. While doing this, possible locking phenomena should be anticipated.

Even though the fracture location was predicted for the ribs with reliable material data, the act of compiling an averaged modelled ribcage require precise and complete data regarding geometry and material properties, particularly for the superior age representation. Here, capturing the effects of aging, such as increased cortical porosity and reduced osteon concentration, is key to fully decipher the structure of the rib. Therefore, further developing the CBM method and, when technology allows, increase the pixel resolution of the CT scans are two suggestible approaches.

Due to the ribs anatomy and osteon orientation, an investigation where an anisotropic material model is applied, should be conducted. The effect of different transverse capabilities could benefit the prediction of the out-of-plane strains and thus, better predict the fracture location.

When expanding the set of ribs to investigate, this thesis suggests that the younger generation, at least below 70 years of age, should be added. This is due to the inability seen in the CBM method and tension test, to give representative input data to the FE model when the cortical bone has been subjected to cortical porosity.

The influence of the simulation setups natural frequency needs to be further evaluated. It was shown in this thesis, that an excitation signal fairly close to the natural frequency govern resonance. The correlation of rib stiffness to natural frequency was established, however only for two ribs. This also raises the question if there is a bias in the physical test setup, as the dynamic response may, in some cases, be unwanted and affects the general evaluation of the ribs.



# Bibliography

- [1] Amanda M. Agnew et al. “The Effect of Age on the Structural Properties of Human Ribs”. In: *Journal of the Mechanical behavior of Biomedical materials* (2015).
- [2] DL Albert et al. “A Comparison of Rib Structural and Material Properties from Matched Whole Rib Bending and Tension Coupon Tests”. In: *Proceedings of the International Research Council on Biomechanics of Injury*. Sept. 2017.
- [3] DL Albert et al. “The Effect of Injurious Whole Rib Loading on Rib Cortical Bone Material Properties”. In: *Proceedings of the International Research Council on Biomechanics of Injury*. 2018.
- [4] Ted Belytschko et al. “Hourglass Control in Linear and Nonlinear Problems”. In: *Computer Methods in Applied Mechanics and Engineering* 43 (May 1984), pp. 251–276.
- [5] M Bischoff et al. “Encyclopedia of Computational Mechanics”. In: vol. 2: Solids and Structures. John Wiley & Sons, 2004. Chap. 3, pp. 59–134.
- [6] Timothy A. Burkhart, David M. Andrews, and Cynthia E. Dunning. “Finite Element Modeling Mesh Quality, Energy Balance and Validation Methods: A Review With Recommendations Associated With The Modeling of Bone Tissue”. In: *Journal of Biomechanics* 46 (2013), pp. 1477–1488.
- [7] Estelle Charpail et al. “Characterization of PMHS Ribs: A New Test Methodology”. In: *Stapp Car Crash Journal* 49 (Nov. 2005), pp. 183–198.
- [8] John D. Currey. *The Mechanical Properties of Bones*. Princeton university press, 2014, pp. 3–87. ISBN: 978-1-4008-5372-4.
- [9] Henry Gray. *Grays Anatomy of the Human Body*. <https://www.bartleby.com/107/>. 1918.
- [10] Brian D. Grenke. *Digital Filtering for J211 Requirements Using a Fast Fourier Transform Based Filter*. Jan. 2002. DOI: 10.4271/2002-01-0796.
- [11] John O. Hallquist. *LS-DYNA® Theory manual*. Livermore Software Technology Corporation. 2006. ISBN: 0-9778540-0-0.
- [12] Elham Hamed, Yikhan Lee, and Iwona Jasiukl. “Characterization of PMHS Ribs: A New Test Methodology”. In: *Acta Mechanica* 213 (Aug. 2010), pp. 131–154. DOI: 10.1007/s00707-010-0326-5.
- [13] Sven A. Holcombe et al. “Measuring Rib Cortical Bone Thickness and Cross Section From CT”. In: *Medical Image Analysis* 49 (Oct. 2018), pp. 27–34.
- [14] Trevor. D Hrynyk and Frank J. Vecchio. “Capturing Out-of-Plane Shear Failures in the Analysis of Reinforced Concrete Shells”. In: *Journal of Structural*

- Engineering* 141 (12 Apr. 2015), pp. 381–427. URL: [https://doi.org/10.1061/\(ASCE\)ST.1943-541X.0001311](https://doi.org/10.1061/(ASCE)ST.1943-541X.0001311).
- [15] LSTC Inc., Dynamore Nordic, and DYNAmore. *New Features in LS-DYNA R10.0*. Dec. 2017. URL: <https://www.dynasupport.com/news/ls-dyna-r10.0.0-r10.118302-released>.
- [16] LSTC Inc., Dynamore Nordic, and DYNAmore Gesellschaft für FEM Ingenieurdienstleistungen mbH. *From engineering to true strain, true stress*. May 2002. URL: <https://www.dynasupport.com>.
- [17] Andrew R. Kemper et al. “The Biomechanics of Human Ribs: Material and Structural Properties from Dynamic Tension and Bending Tests”. In: *Stapp Car Crash Journal* (2007).
- [18] A.R Kemper et al. “Material Properties of Human Rib Cortical Bone from Dynamic Tension Coupon Testing”. In: *Stapp Car Crash Journal* (2005).
- [19] Matthew W. Kindig. “Tolerance To Failure and Geometric Influences on the Stiffness of Human Ribs Under Anterior-Posterior Loading”. MA thesis. School of Engineering and Applied Science University of Virginia, Oct. 2009.
- [20] Henry L. Langhaar. Dover Publications, 2016. ISBN: 978-0-486-81113-0. URL: <https://app.knovel.com/hotlink/toc/id:kpEMAM000B/energy-methods-in-applied/energy-methods-in-applied>.
- [21] Zuoping Li et al. “Rib Fractures Under Anterior-Posterior Dynamic Loads: Experimental and Finite-Element Study”. In: *Journal of biomechanics* (2010).
- [22] Zuoping Li et al. “Influence of Mesh Density, Cortical Thickness and Material Properties on Human Rib Fracture Prediction”. In: *Medical Engineering & Physics* (2010).
- [23] Amine Maida. “Modélisation Des Côtes Humaines en Flexion Antéropostérieure”. MA thesis. Chalmers University of Technology and The Institut Scientifique et Polytechnique Galilée, 2017.
- [24] Marcus Mohr et al. “Geometry of Human Ribs Pertinent to Orthopedic Chest-Wall Reconstruction”. In: *Journal of Biomechanics* (2007).
- [25] Carlos A. de Moura and Carlos S. Kubrusly. *The Courant-Friedrichs-Lewy (CFL) Condition*. Springer Science+Business Media New York, 2013, pp. 1–7. ISBN: 978-0-8176-8394-8. DOI: 10.1007/978-0-8176-8394-8\_1.
- [26] Rafal Perz, Jacek Toczyski, and Damien Subit. “Variation in the Human Ribs Geometrical Properties and Mechanical Response Based on X-ray Computed Tomography Images Resolution”. In: *Journal of the Mechanical Behavior of Biomedical Materials* (2014).
- [27] Kenneth Runesson. *Constitutive Modeling of Engineering Materials Theory and Computation*. Lecture Notes, Dept. of Applied Mechanics, Chalmers University of Technology. Mar. 2006.
- [28] Leonard E. Schwer et al. “An Assessment of the LS-DYNA Hourglass Formulations via the 3D Patch Test”. In: *5th European LS-DYNA Users Conference - Code development*. 2005.
- [29] U Stelzmann. “Die Grösse Elementbibliothek in LS-DYNA - Wann Nimmt Man Was?” In: *Tech. rep.* 2010.
- [30] Télécom Paris Tech and Électricité de France S.A. *CloudCompare 2.9.1*. <https://www.danielgm.net/cc/>. 2017.



- [31] Carsten Thunert. *CORA Release 3.6 User's Manual*. Sept. 2012. URL: <http://www.pdb-org.com/en/>.
- [32] Epidemiology U.S. National Cancer Institute's Surveillance and End Results (SEER) Program. *Compact bone & spongy bone*. 2011. URL: [https://en.wikipedia.org/wiki/Bone#/media/File:Illu\\_compact\\_spongy\\_bone.jpg](https://en.wikipedia.org/wiki/Bone#/media/File:Illu_compact_spongy_bone.jpg).



# A

## Appendix 1

## A.1 Energy balance evaluation

The metrics used to assess the energy balance as well as the mass increase from the mass scaling is presented in Table A.1.

**Table A.1:** Energy balance and mass scaling evaluation

Rib	Approach	Max( energy ratio )	Max( $\frac{\text{HG energy}}{\text{Total energy}}$ )[%]	Mass increase [%]
Rib A	AHM	1.001	0.04	2.50
	AHV	1.001	0.03	2.45
Rib B	AHM	1.001	0.04	2.53
	AHV	1.001	0.03	2.40
Rib C	AHM	1.001	0.04	2.69
	AHV	1.001	0.03	2.68
	HTS	14.47	0.26	1.88
	HS	1.001	0.03	2.42
Rib D	AHM	1.001	0.04	1.90
	AHV	1.001	0.03	1.89
Rib E	AHM	1.001	0.08	1.48
	AHV	1.001	0.04	1.49
	HTS	1.315	3.03	2.09
	HS	1.002	0.05	2.42
Rib F	AHM	1.001	0.04	2.34
	AHV	1.001	0.03	2.30
	HTS	1.206	0.81	2.04
	HS	1.001	0.03	1.65
Rib G	AHM	1.001	0.09	2.04
	AHV	1.001	0.05	1.99
Rib H	AHM	1.001	0.08	2.67
	AHV	1.001	0.04	2.63
	HTS	1.690	1.41	0.86
	HS	1.001	0.07	0.87
Rib I	AHM	1.001	0.12	3.14
	AHV	1.001	0.07	3.10
	HTS	1.295	1.90	2.18
	HS	1.001	0.08	2.60
Rib J	AHM	1.001	0.07	2.20
	AHV	1.001	0.04	2.16
	HTS	-	-	-
	HS	1.001	0.05	2.27
Rib K	AHM	1.001	0.08	2.88
	AHV	1.001	0.07	2.78
	HTS	-	-	-
	HS	1.000	0.06	1.87
Rib L	AHM	1.001	0.09	2.72
	AHV	1.001	0.04	2.52

## A.2 Simulation-Validation plots

The numerical and experimental curves are presented without any time-shift alterations to allow the reader to compare the data for him or herself .

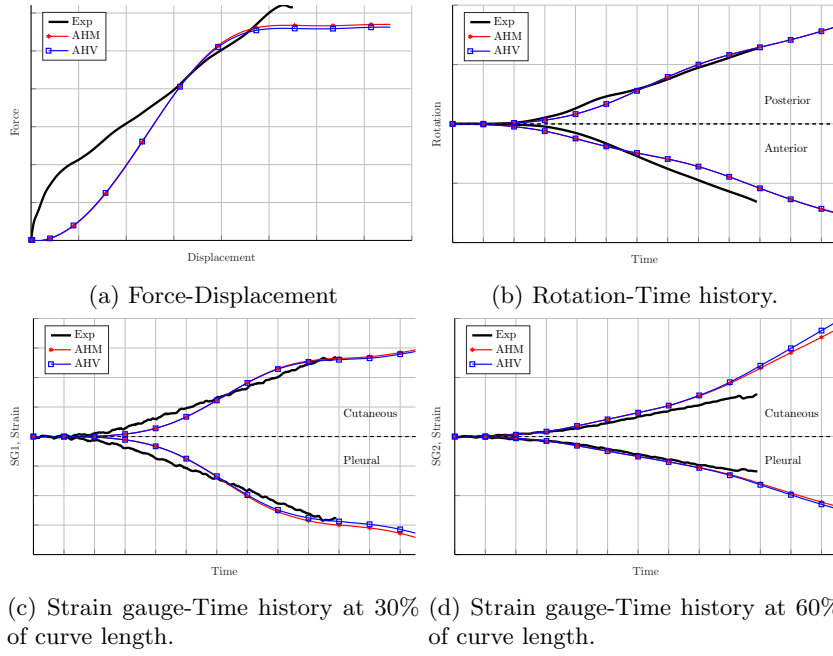


Figure A.1: Simulation comparison with experiments for Rib A.

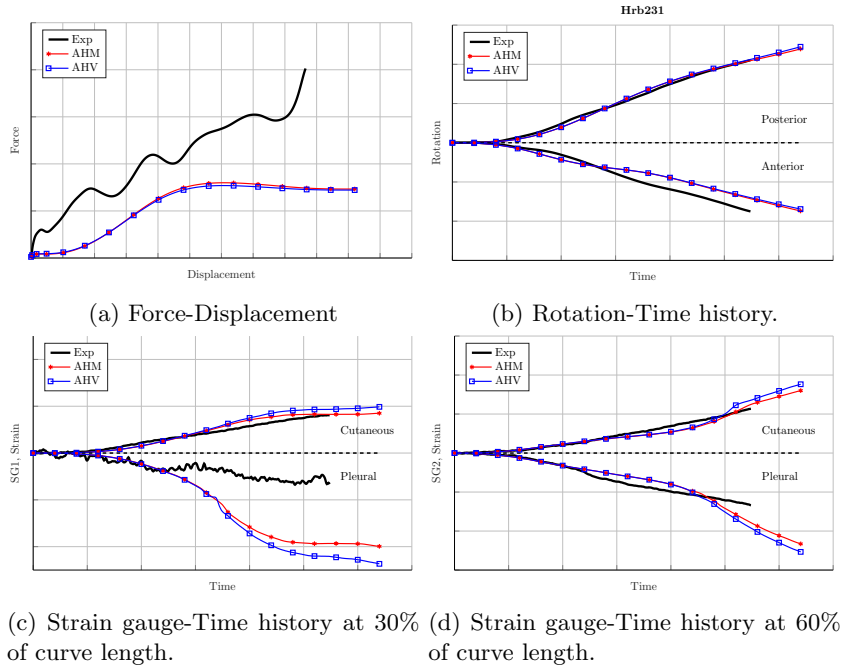


Figure A.2: Simulation comparison with experiments for Rib B.

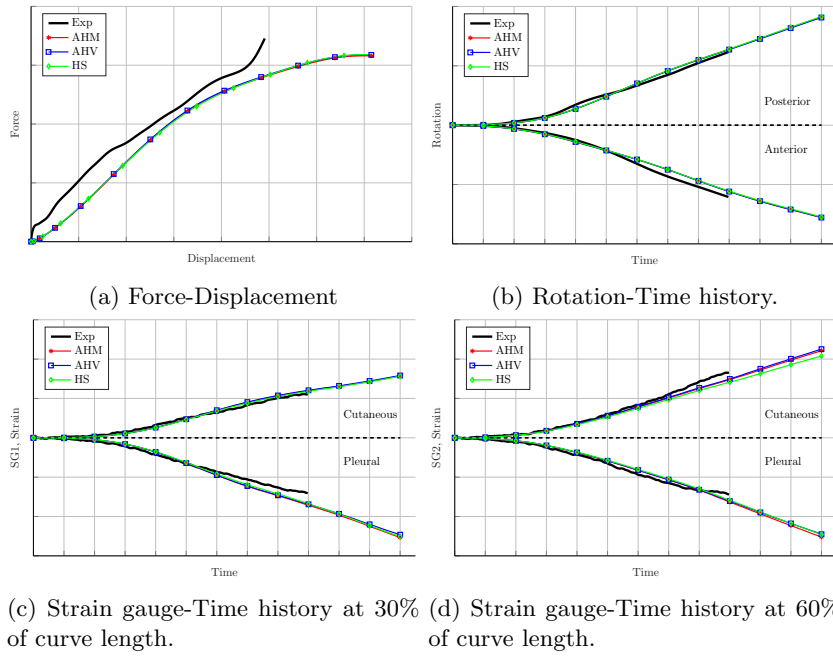


Figure A.3: Simulation comparison with experiments for Rib C.

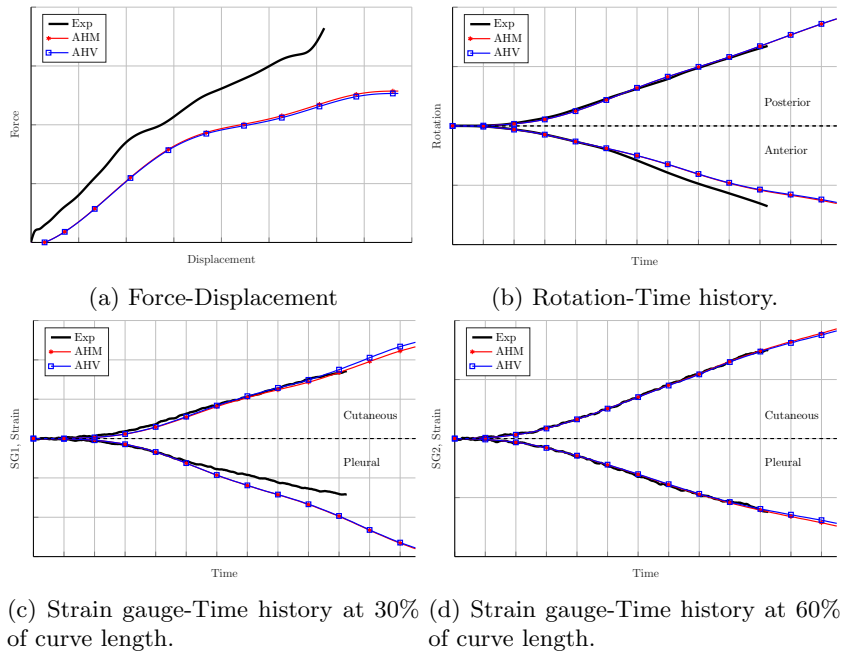


Figure A.4: Simulation comparison with experiments for Rib D.

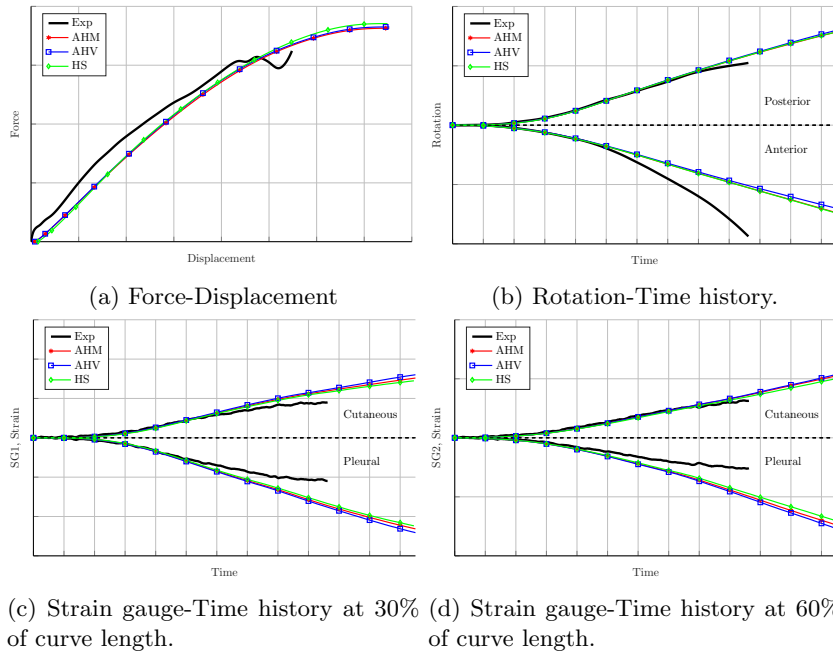


Figure A.5: Simulation comparison with experiments for Rib E.

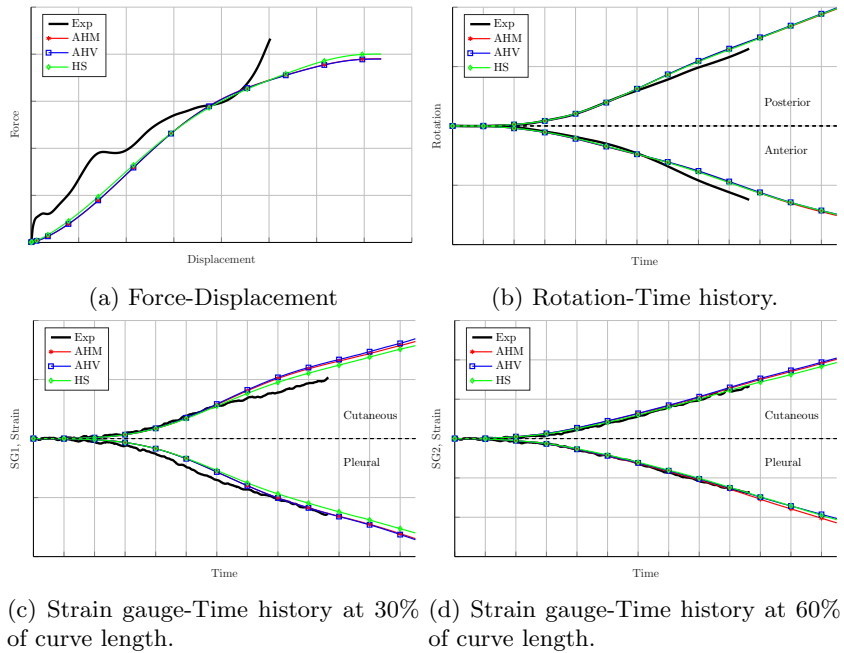


Figure A.6: Simulation comparison with experiments for Rib F.



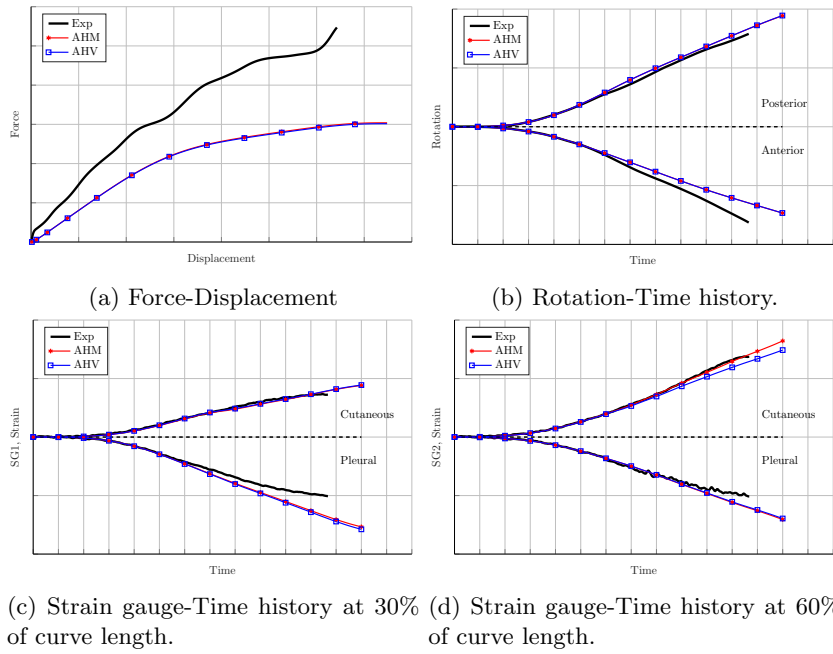


Figure A.7: Simulation comparison with experiments for Rib G.

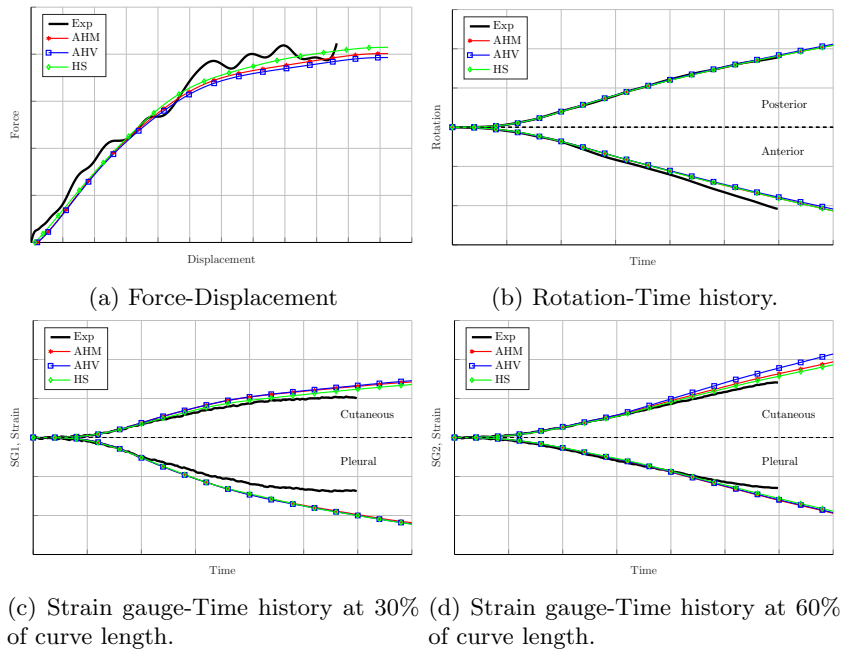


Figure A.8: Simulation comparison with experiments for Rib H.

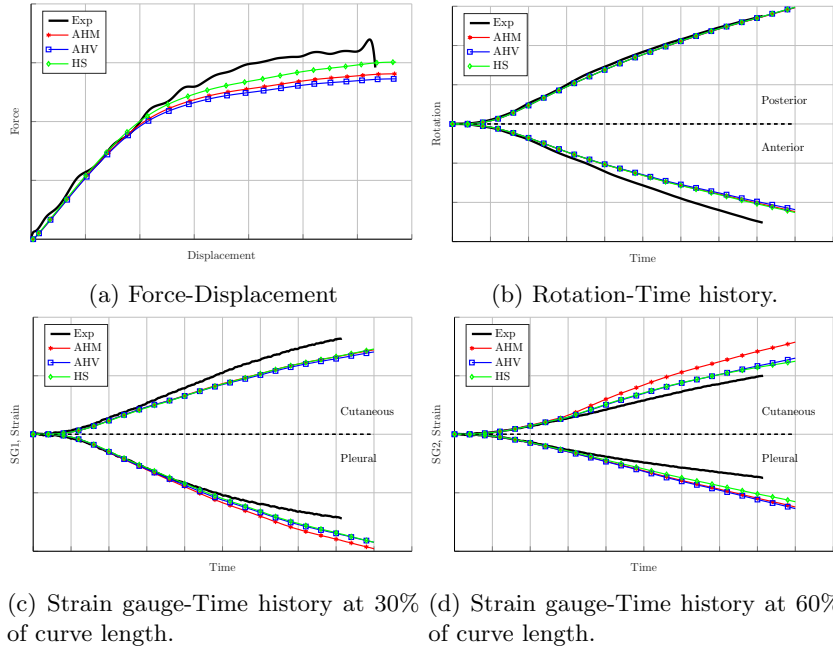


Figure A.9: Simulation comparison with experiments for Rib I.

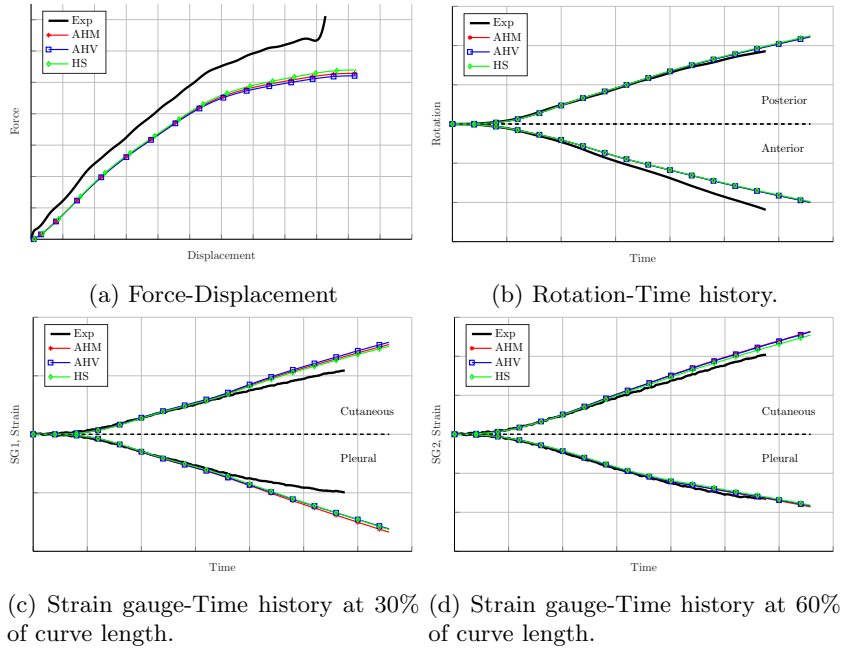


Figure A.10: Simulation comparison with experiments for Rib J.

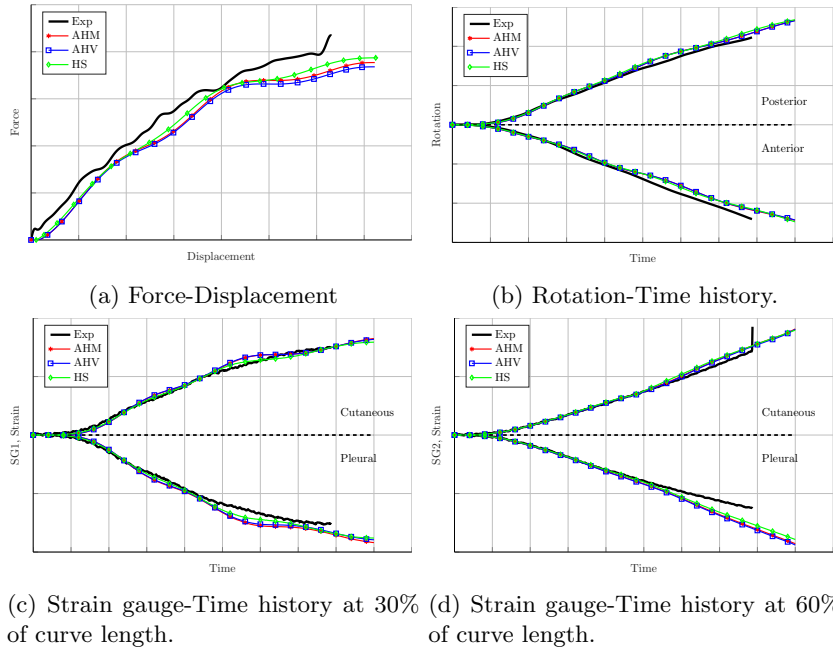


Figure A.11: Simulation comparison with experiments for Rib K.

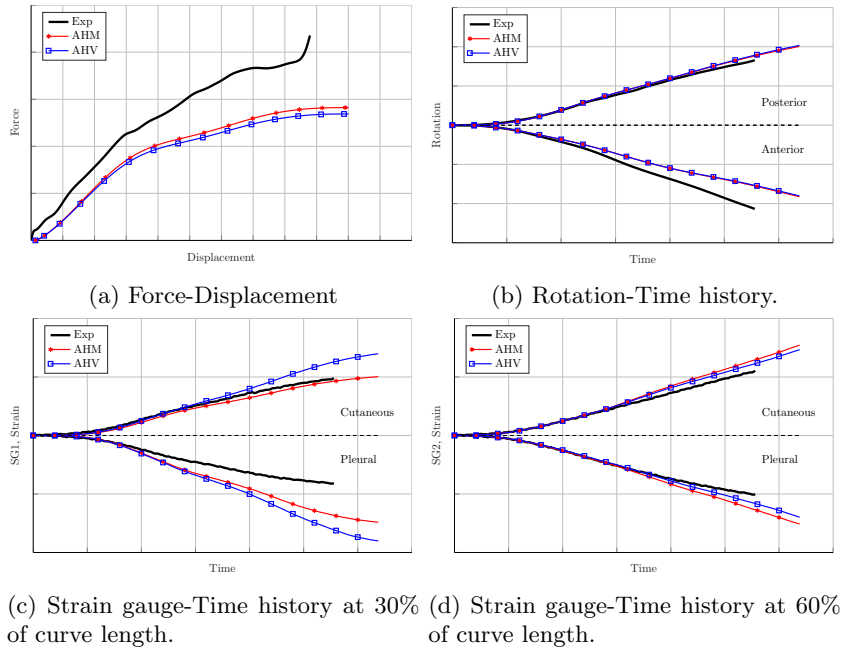


Figure A.12: Simulation comparison with experiments for Rib L.